The Meteoritical Society

Meteoritics & Planetary Science 59, Nr 12, 3250–3281 (2024)
doi: 10.1111/maps.14275

Shock petrographic and numerical modeling constraints on the morphology and size of the Morokweng impact structure, South Africa

Roger L. GIBSON[1]*, S'lindile S. WELA[1], Auriol S. P. RAE[2,3], and Marco A. G. ANDREOLI[1]

[1]School of Geosciences, University of the Witwatersrand, Johannesburg, South Africa
[2]Department of Earth Sciences, University of Cambridge, Cambridge, UK
[3]School of GeoSciences, University of Edinburgh, Edinburgh, UK

***Correspondence**
Roger L. Gibson, School of Geosciences, University of the Witwatersrand, PO WITS, Johannesburg 2050, South Africa.
Email: roger.gibson@wits.ac.za

(Received 28 October 2023; revision accepted 08 October 2024)

Abstract–The 369 m deep M4 drill hole, located ~18 km NNW of the center of the 146 Ma Morokweng impact structure (MIS), intersects shocked Archean granitoid gneisses and subsidiary dolerite intrusions that are cut by faults, cataclasites and mm- to m-wide suevitic and pseudotachylitic breccia dikes. The shock features in quartz in the gneisses and breccia dikes include decorated planar deformation features (PDFs), planar fractures, feather features, and toasting. Other minerals show features that may be shock-related, such as multiple sets of planar features and alternate twin ladder structures in feldspars, kink bands in biotite, and planar features in titanite, apatite, and zircon; however, these are variably annealed and/or overprinted by hydrothermal alteration effects, and confirmation of their origin awaits further study. Universal Stage measurements of PDF sets in quartz from 12 gneissic target rocks and from lithic and mineral clasts in three suevitic and three pseudotachylitic breccia dikes reveal four dominant sets: (0001), $\{10\bar{1}3\}$, $\{10\bar{1}4\}$ and $\{10\bar{1}2\}$. Based on these observations, the average peak shock pressure in these rocks is estimated at ≤16 GPa, which supports the original proximity (within one transient cavity radius) of these rocks to the point of impact. No discernible depth-dependent shock attenuation was noted in the core. These shock levels and the elevated structural position of the rocks in the M4 core relative to the impact melt sheet intersected in drill holes closer to the center of the MIS suggest that the M4 lithologies represent part of the parautochthonous peak ring volume that subsequently experienced 1.5–2 km of post-impact erosion before it was buried beneath younger sediments. Numerical modeling using the iSALE-2D code suggests that the original Morokweng crater had a rim-to-rim diameter of between 70 and 80 km, and that the rocks in the M4 core were originally located at a depth of 7–8 km and a radial distance of 8–9 km from the point of impact.

INTRODUCTION

Unlike their smaller counterparts, large impact craters are characterized by complex collapse kinematics that significantly redistribute and disrupt the central crater basement containing the most highly shocked rock volume (Melosh, 1989; Melosh & Ivanov, 1999). As a result, the final disposition of the shock isobars in the crater basement rocks beneath the allochthonous crater fill breccias can be significantly modified from its initial, approximately concentric, radially attenuating, pattern. Understanding this collapse-related redistribution of material and shock evidence is critical in constraining crater size, impact parameters, and fundamentally, the manner in which Earth's crust responds to the extreme stress and strain conditions imposed by hypervelocity collisions (e.g., Rae et al., 2021). However, unlike most other solid bodies in the Solar System, Earth's surface is highly dynamic and is subjected to erosion, burial, and/or tectonic disruption, which can modify, destroy, or obscure some or all of the key surface morphological and shallow-lying crater fill features that are central to determining these parameters (Kenkmann, 2021). These issues are well illustrated by the large uncertainties in original crater diameter (and therefore impact energy release) and crater morphology for the three largest (>150 km) terrestrial impact craters, namely, Vredefort (eroded), Sudbury (deformed and differentially eroded) and Chicxulub (buried) (e.g., Grieve et al., 2008; Ivanov, 2005). Among the next four largest impact structures on Earth (www.passc.net/earthimpactdatabase), Popigai (Russia—100 km; Masaitis et al., 1999, 2005) and Manicouagan (Canada—85 km; Thompson & Spray, 2017) are only slightly eroded yet appear to have somewhat different morphologies, whereas Acraman (Australia) is too deeply eroded to obtain reliable estimates of its diameter and details of its morphology (Williams & Schmidt, 2021). The fourth—Morokweng, in South Africa—is both partially eroded and buried, such that estimates of its diameter have varied from 65 km (Henkel et al., 2002) to as much as 340 km (Corner et al., 1997; Hart et al., 1997). In this article, we combine lithological and shock petrographic evidence from a drill core in the Morokweng impact structure (MIS) with numerical modeling to argue that the drill core intersects part of the parautochthonous peak ring of a crater that had an original apparent rim diameter of between 70 and 80 km.

GEOLOGICAL SETTING

Morokweng was first proposed as an impact structure by Andreoli et al. (1995) and subsequently by Corner et al. (1997), who recognized a 65–70 km wide annular magnetic anomaly in rocks buried beneath up to 200 m of Late Cretaceous to Cenozoic sediments in the southern part of the Kalahari Basin (Figure 1a). They also reported planar deformation features (PDFs) in quartz from a drill core and two surface samples. In the geophysical data, Corner et al. (1997) and Hart et al. (1997) distinguished between an inner, 25–35 km wide, circular to slightly N-S elongate, up to 350 nT, positive magnetic anomaly, and an outer, 15–20 km wide, annulus in which the prevailing magnetic fabric in the Archean-Paleoproterozoic basement is subdued and severely disrupted. Although Corner et al. (1997), Hart et al. (1997), and Andreoli et al. (2007, 2008) speculated that several further partial concentric geophysical anomalies at greater radial distances might indicate a diameter of as much as 240–340 km for the impact structure, Henkel et al. (2002) argued that its apparent rim diameter is restricted to the principal, 65–70 km wide, geophysical anomaly. Reimold et al. (2002) also supported the smaller diameter based on a general lack of evidence of impact-diagnostic features in the 3.2 km deep KHK-1 exploration drill core located ~40 km southwest of the center of the magnetic anomaly (Figure 1a), although the shallowest 600 m of the stratigraphy, which was transected using percussion drilling, was discarded prior to their study.

Four of five exploration cores drilled in the 1980s and 1990s into the central geophysical anomaly of the MIS intersected a clast-laden, differentiated, granophyric-textured, norite body that geochronological and geochemical studies confirmed is a 146.06 ± 0.16 Ma (Kenny et al., 2021; see also Hart et al., 1997; Koeberl et al., 1997) impact melt sheet. The melt sheet is significant for carrying an up to 5% extraterrestrial component (Koeberl et al., 1997; Koeberl & Reimold, 2003), and unusually, fragments of the LL6 chondritic meteorite impactor (Maier et al., 2006). Henkel et al. (2002) linked the central magnetic high to the geographic extent of this impact melt sheet and possibly underlying magnetized basement and interpreted the adjacent annulus of subdued and disrupted magnetic signals as the product of structural disturbance of the crater basement by impact-induced slump faulting and brecciation, and oxidation of ferrimagnetic mineral phases by post-impact hydrothermal alteration. They postulated that the absence of a positive central gravity anomaly favors a smaller crater diameter than had previously been proposed and that the amount of structural uplift in the center of the MIS was limited to ~4 km. Of the four central drill holes (Figure 1), only the M3 hole appears to have intersected the footwall beneath the melt sheet, which mainly comprises Archean granitoid and amphibolitic gneisses at this locality (Figure 1b; Hart et al., 2002; Kenny et al., 2021). The M3 core intersects ~800 m of melt sheet, however, the upper chill margin and crater fill fallback breccias are missing in all four drill cores, indicating significant erosion of the crater prior to deposition of the younger sedimentary cover.

The 369 m deep M4 hole, located at 26°21.3158′ S, 23°27.8529′ E, was drilled in 1998–1999, ~6 km WNW of the M3 hole (Figure 1a). The regional outcrop pattern (Figure 1a) and presence of quartzite clasts in the melt sheet (Andreoli et al., 1999; Hart et al., 1997; Reimold et al., 1999) suggest that at least some part of the target crust may have included some metasediments and metavolcanics of the Paleoproterozoic Griqualand West and Olifantshoek supergroups, and/or Phanerozoic Karoo Supergroup sediments and volcanics (e.g., Henkel et al., 2002; Westgate et al., 2021). However, the M4 core comprises only Archean granitoid gneisses, with subsidiary metadolerite and dolerite (Wela, 2017; Gibson et al., 2022; Figure 1b). The granitoid gneisses, metadolerite, and dolerite lie beneath 94 m of Kalahari Group clay, calcrete, and sand, and are shocked, highly faulted, locally

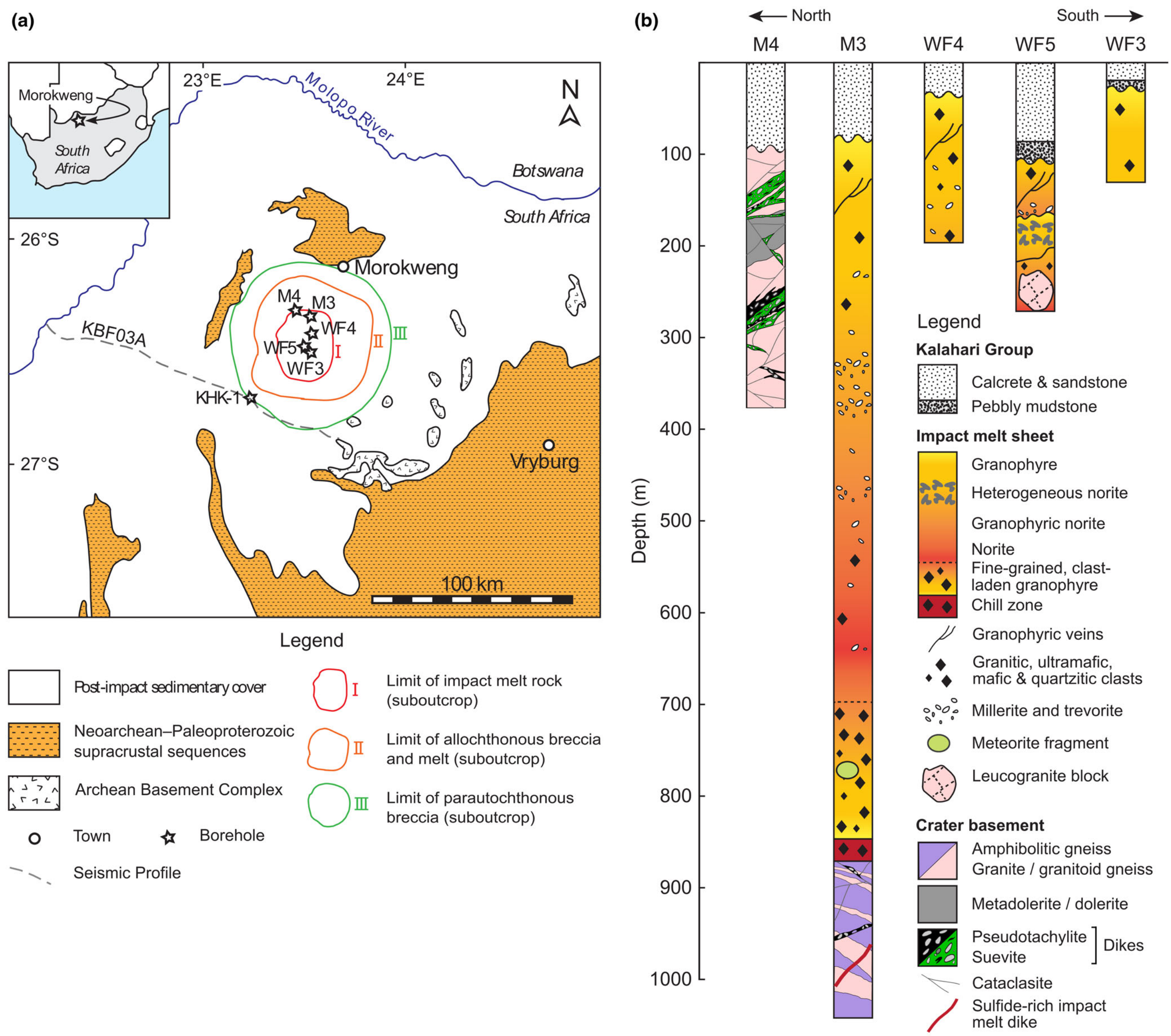

FIGURE 1. (a) Simplified geological map of the buried Morokweng impact structure showing the interpreted limits of the principal geophysical features (modified after Hart et al., 2002) and locations of the principal boreholes and seismic section line referred to in the text. (b) Simplified logs of the five principal exploration drill cores from the central parts of the MIS (modified after Hart et al. (2002) and Wela (2017)). (Color figure can be viewed at wileyonlinelibrary.com)

cataclased, and host mm- to m-wide pseudotachylite and suevite dikes (Figures 1b and 2; Gibson et al., 2024; Wela, 2017). The major lithological contacts in the core are marked by evidence of faulting/shearing, brecciation or local core loss, suggesting that they have been structurally modified; nonetheless, the general uniformity of the steep gneissic foliation throughout the drill core (Gibson et al., 2022) suggests a largely coherent rock mass, rather than a megabreccia. All rock types in the drill core have been affected by post-impact zeolite–smectite alteration and hydrothermal veining. Evidence of brittle–ductile shearing and related quartz veining predating the impact shock occurs in granitoid gneiss and metadolerite between 201 and 260 m depth (Wela, 2017).

Macroscopic investigation of slightly parabolic striated fracture surfaces in the 4.5 cm diameter core revealed some variability in lineation orientations on individual fractures, but no compelling evidence that these represent shatter cones such as those identified by Morgan et al. (2016) in the M0077A core from the Chicxulub impact crater. Shock evidence is thus exclusively based on transmitted light microscopy. Bulk-powder XRD analysis

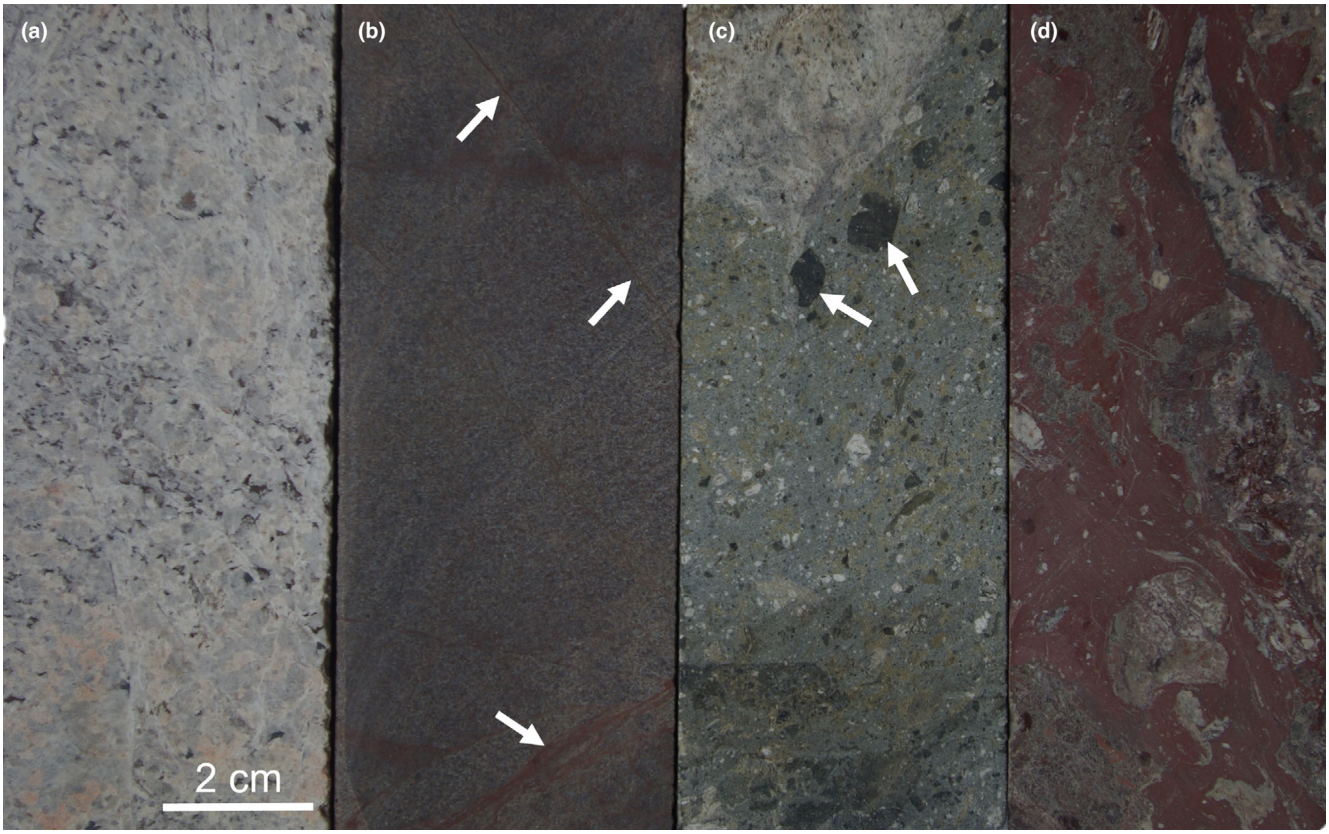

FIGURE 2. Representative lithologies in the M4 drill core. (a) Granitoid gneiss with subvertical zeolite-bearing cataclasite fracture network (261.4 m depth). (b) Metadolerite showing mm-wide pseudotachylite dikes (arrows) (268.0 m depth). (c) Suevite dike showing large cataclased granitoid gneiss clast at top, and angular fragments of melt (arrows) (223.7 m depth). (d) Pseudotachylite showing a steep flow foliation defined by streaky, boudinaged and locally folded, cataclastic aggregates derived from granitoid gneiss (top, right) and dolerite (top, left), and mm- to cm-scale mineral clasts (272 m depth). (Color figure can be viewed at wileyonlinelibrary.com)

did not reveal any evidence of high-pressure polymorphs of quartz, graphite, or zircon (Wela, 2017).

METHODOLOGY

A total of 98 thin sections from 70 samples (37 target rocks, 33 suevitic and pseudotachylitic breccias) from the M4 core were examined via transmitted and reflected light microscopy, complemented by targeted backscatter electron (BSE) scanning electron microscopy to identify mineral textures, modal mineral abundances, alteration effects and microscopic shock metamorphic features. Of these, 18 thin sections were selected for PDF orientation analysis in quartz grains using a Leitz 4-axis universal stage microscope, according to the techniques described in Engelhardt and Bertsch (1969), Stöffler and Langenhorst (1994) and Ferrière et al. (2009). As all but three of the quartz-bearing samples display PDFs, the selection for PDF analysis aimed primarily to cover the full depth range of the core and to allow comparison between all target and impact lithologies. The analysis involved repeat measurements of the orientation of the c-axis (optic axis) and poles for all PDF sets in each quartz grain. Data were then input into the ANIE v1.0 program (Huber et al., 2011) to index the PDFs. Manual cross-checking of the indexed results was done via the new stereographic projection template (NSPT) of Ferrière et al. (2009). In plotting the data, a 5° error envelope was assigned to account for measurement errors and small amounts of lattice distortion in the host grain. This creates an overlap specifically between the $\{10\bar{1}3\}$ and $\{10\bar{1}4\}$ orientations, which was acknowledged by considering all data in this range to refer to $\{10\bar{1}3\}$ in the final analysis.

A key consideration in the quartz PDF shock barometry technique is the collection of a statistically valid data set (Ferrière et al., 2009), although the minimum number of grains needed is a matter of some debate (e.g., French & Koeberl, 2010; Holm-Alwmark et al., 2018). Wherever possible, an attempt was made to measure 20 grains per thin section. The low number generally reflects the coarse grain size and the common occurrence of internal strain (undulose extinction, deformation bands, tiltwalls, fractures, and grain scale brecciation) in quartz in the granitoid gneisses, the paucity of quartz in the doleritic rocks, and/or the limited number of viable quartz-bearing clasts in the pseudotachylitic and suevitic breccias. In two samples, measurements were performed on more than one thin section in an attempt to obtain additional data, owing to the small number of quartz grains per thin section that contained measurable PDF sets. Shock pressure estimates were derived from the PDF orientations using the method of Robertson and Grieve (1977), according to the classification scheme of Stöffler and Langenhorst (1994), Grieve et al. (1996), and Holm-Alwmark et al. (2018).

Numerical simulations of the Morokweng impact were performed using the multirheology, multimaterial, iSALE-2D shock physics code, which is based on the original SALE hydrocode of Amsden et al. (1980). iSALE incorporates an elastoplastic constitutive model, fragmentation models (Melosh et al., 1992), a variety of equations of state (Ivanov et al., 1997), a porous compaction model (Wünnemann et al., 2006) and a dilatancy model (Collins, 2014). It has been used increasingly in recent years to model complex impact structures such as Chesapeake Bay (Collins & Wünnemann, 2005; Kenkmann et al., 2009), Sierra Madera (Goldin et al., 2006), Haughton and El'gygytgyn (Collins, Kenkmann, et al., 2008), Serra de Cangalha (Vasconcelos et al., 2012), Vista Allegre (Vasconcelos et al., 2019), Ries (Artemieva et al., 2013), Siljan (Holm-Alwmark et al., 2017), West Clearwater (Rae et al., 2017), and Chicxulub (Rae et al., 2019).

The aim of numerical modeling in this study was to produce a range of crater sizes that could be compared against the observations of the M4 drill core and previously published geophysical data. A variety of scenarios involving different impactor diameters, velocities, angles of obliquity, and target stratigraphy were investigated initially. First, it was found that the inclusion of a 1.5 km thick meta-sedimentary rock upper layer overlying the granitoid basement (representing likely Proterozoic and Phanerozoic supracrustal sequences known in the region) produced negligible changes in crater structure and melt volume. Consequently, the simulations presented here involve only a uniform granite crust. Additionally, while the MIS was formed by an LL6 chondrite (Maier et al., 2006), a granite projectile was used to generate the modeled craters for several reasons. First, reducing the number of materials within the simulation improved computational efficiency. Second, the structure of a given complex crater is determined by the size of the transient crater that collapses, which in turn is determined by the projectile size, velocity, angle, and density. These parameters trade-off against each other, and so, while projectile material could be varied, only a comparatively small change in projectile size or velocity would compensate for the change in projectile materials, given the constraint that the projectile was stony in composition. Consequently, we have adopted the simplest modeling scenario (see also Collins, Morgan, et al. 2008; Holm-Alwmark et al., 2017; Rae et al., 2017, 2019). Lagrangian tracer particles were used to track the history of material packages (e.g., Collins, Morgan, et al. 2008; Pierazzo et al., 1997). The main model parameters are presented in Table 1 and input files for the simulations are provided in the Supporting Information.

RESULTS

Petrographic Analysis of Impact-Related Microdeformation Features

Impacts produce microdeformation effects within the constituent minerals in target rocks as a result of both shock passage (e.g., French, 1978; Stöffler, 1972) and crater-excavation and -modification. This section describes both bona fide shock features and other intragranular features in the rocks of the M4 drill core that are interpreted as impact-related.

Quartz

Quartz is present as grains up to a few mm in size in the granitoid gneisses; in the metadolerite, quartz occurs in fine-grained (<0.1 mm) aggregates intergrown with plagioclase, and in dolerite samples, it is only present in rare interstitial granophyric intergrowths. Decorated PDFs are the most common shock feature. The PDFs in the gneisses are typically found in 1–3 (rarely 4–5) sets per grain and are defined by closely spaced (≤5 μm) planar trails of micron-sized fluid inclusions (Figure 3a,b). The PDFs may cut across the entire grain but are more commonly irregularly distributed within individual grains. The densest arrays and greatest number of sets are typically (but not exclusively) found close to grain edges.

The PDFs are mostly planar, but curved PDFs (Figure 3c) are relatively common and are found in grains that display undulose extinction; sharper deflections coincide with the edges of deformation bands and/or tiltwalls. These features are attributed primarily to strain linked to impact-related fault movements that followed the shock wave (Gibson et al., 2024), but some internal strain features (undulose extinction, deformation bands, subgrains) are related to the brittle–ductile pre-impact fault zone recognized in the metadolerite and trondhjemitic gneiss at intermediate depths in the core. In the granitoid rocks, in situ "jigsaw microbrecciation" of PDF-bearing quartz grains, in which the PDF sets in individual fragments may show limited to no relative rotations, is quite common (Figure 3d). The fragments are separated by hydrothermal zeolite, phyllosilicates, pyrite,

TABLE 1. Model parameters used in impact simulations.

Parameter	Value	
Cell resolution	50, 75, **100**, 125, 150 m	
Cells per projectile radius	30, 36, 42	
Impactor velocity	**11.2**, 15.0, 20.5 km s^{-1}	
Impactor density	2670 kg m^{-3}	
Acceleration due to gravity	9.81 m s^{-2}	
Surface temperature	288 K	
Surface temperature gradient	1.2E-2 k m^{-1}	
Lithospheric thickness	120 km	
	Crust	Mantle
Equation of state	Granite (Pierazzo et al., 1997)	Dunite (Benz et al., 1989)
Layer thickness	39 km	–
Reference density	2670	3320
Poisson's ratio	0.30	0.25
Intact cohesive strength	10 MPa	10 MPa
Intact friction coefficient	2.0	1.2
Intact and damaged strength limit	2500 MPa	3500 MPa
Damaged cohesive strength	0.01 MPa	0.01 MPa
Damaged friction coefficient	0.6	0.6
Minimum failure strain for low pressure states	1.0E−4	1.0E−4
Constant of proportionality between failure strain and pressure	1.0E−11	1.0E−11
Pressure above which failure is compressional	300 MPa	300 MPa
Melt temperature	1673	1373 K
Thermal softening coefficient	1.2	1.2
Constant in Simon approximation	6.0E9	1.52E9
Exponent in Simon approximation	3.00	4.05
γ_η	**1.75E−2**, 2.04E−2, 2.45E−2	**1.75E−2**, 2.04E−2, 2.45E−2
γ_β	**150**, 175, 210	**150**, 175, 210
Vibrational particle velocity as a fraction of particle velocity	0.1	0.1
Maximum vibrational particle velocity	200 m s^{-1}	200 m s^{-1}
Time after which no new acoustic vibrations are generated	16 s	16 s
Maximum dilatancy coefficient	0.09	0.09
Dilatancy pressure limit	200 MPa	200 MPa
Critical distension	1.2	1.2
Critical friction coefficient	0.4	0.4
Initial distension	1.0	1.0
Minimum distension	1.0	1.0

Note: Parameters that appear to produce the best-fit simulation are in bold.

and/or magnetite–hematite fill, which also locally replaces the PDFs (Figure 3a). Progressive disruption and rotation of original quartz grains containing PDFs occurs alongside cataclasite, indicating that cataclasis followed shock (Figure 3d). In pseudotachylite, quartz clasts commonly display evidence of recrystallization to fine- to medium-grained aggregates that may retain only small relics showing PDFs; this recrystallization is attributed to a combination of strain-related grain size reduction (dynamic recrystallization) caused by impact-induced shear and heat derived from the cooling friction melt (Gibson et al., 2024; Wela, 2017). Polycrystalline quartz clasts up to several mm in size in the suevite and pseudotachylite are derived from the pre-impact quartz veins; clasts as small as 50 μm may contain PDFs; however, quartz clasts in the suevite and pseudotachylite dikes generally show fewer sets than the granitoid gneisses (see Tables 2 and 3 and Figure 6).

In addition to containing multiple sets of decorated PDFs, quartz in the granitoid gneisses displays intragranular fractures, including feather features (Figure 3e). Feather features comprise relatively short, subparallel fractures that branch off asymmetrically from a larger planar fracture (Poelchau & Kenkmann, 2011). They can form at relatively low shock pressures in conjunction with shearing along planar fractures that are oriented ~45° to the shock propagation direction (Ebert et al., 2020; Poelchau & Kenkmann, 2011). Up to three

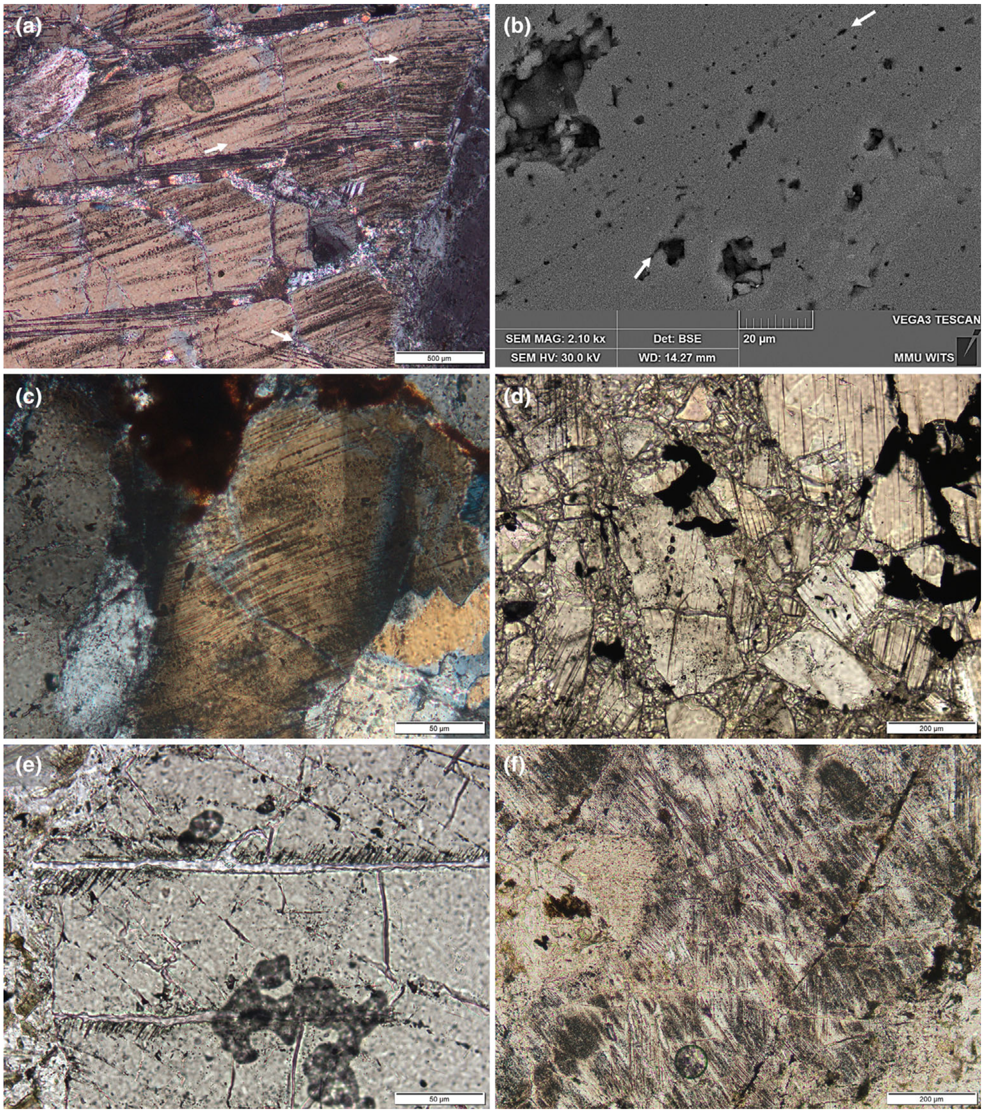

FIGURE 3. Shock-induced features in quartz in the M4 drill core. (a) Three sets of decorated PDF, indicated by arrows, are cut by irregular fractures containing hydrothermal phyllosilicates, which also partially replace closely spaced PDF arrays (Crossed-polarized light (XPL), sample GG8, 152 m depth). (b) Backscattered electron (BSE) image showing micron-sized fluid inclusion cavities along two PDF sets. Larger cavities containing hydrothermal minerals also preferentially exploit the PDF orientations (sample R8, 348 m depth). (c) Curved PDF in strained quartz (XPL, sample FZ2b, 219 m depth). (d) Edge of large quartz grain (right) against cataclasite showing progressive disruption and rotation of PDF-bearing fragments. Hydrothermal pyrite (black) cements fragments on the right that fit together in a jigsaw pattern (plane-polarized light—PPL, sample GG15, 324 m depth). (e) Feather features preferentially replaced by zeolite. Note the scalloped walls of the feather features, indicating growth of zeolite at the expense of the host quartz grain (PPL, sample SB3.2, 355 m depth). (f) Variable toasting in quartz, attributed to dense microinclusions along PDF sets (PPL, sample R9, 346 m depth). (Color figure can be viewed at wileyonlinelibrary.com)

sets of intragranular planar to subplanar fractures spaced up to tens of microns apart occur in quartz grains, but curved and Herzian fractures are also present locally. The former is not as intense as the "pervasive subgrain-scale fracturing" noted by Rae et al. (2019) in the Chicxulub M0077A core, but their planar nature suggests orientation along rational crystallographic planes, which is a common characteristic of shock-induced fractures in quartz. They differ from dilational and shear fractures related to the impact-induced faulting, which are intergranular, associated with larger displacements, and contain wider hydrothermal mineral fill. The extent of replacement of all planar features in quartz is highly variable in the M4 core. Both planar fractures and feather features—and in some cases even PDFs—are locally partially replaced by zeolite, relatively coarse but dendritic calcite, or neoblastic

TABLE 2. Crystallographic orientation abundances of PDFs (%) derived from universal stage measurements of shocked quartz grains in target rocks in the M4 drill core, Morokweng impact structure.

Rock type		Granodioritic Gneiss	Granitic Gneiss	Metadolerite (Silicified)	Trondhjemitic Gneiss	Trondhjemitic Gneiss	Granitic Gneiss	Granitic Gneiss	Monzonitic Gneiss	Monzonitic Gneiss	Monzonitic Gneiss	Granodioritic Gneiss	Monzonntic Gneiss
Sample no.		M4 GG-4	M4 GG-2	M4 IS-2	M4 FZ-2	M4 FZ-4	M4 GG-17	M4 GG-3	M4 AM-2	M4 AM-1	M4 AM-4	M4 GG-16	M4 AM-5
Depth (m)		109.20	131.90	211.41	219.30	233.5	274.15	306.00	338.15	340.70	359.7	360.3	362.63
Number of investigated grains (n)		20	20	18	20	21	18	20	10	10	20	20	20
Number of measured sets (Q)		40	44	36	40	30	37	39	18	17	33	38	31
Number of PDF sets/grain (Q/n)		2	2.2	2	2	1.4	2.1	2	1.8	1.7	1.7	1.9	1.6
Polar angles and PDF crystallographic orientations		Absolute frequency (%)											
0.00°	c (0001)	35	20	36	33	57	38	23	33	35	9	34	19
	$\{10\bar{1}4\}/\{10\bar{1}3\}$[b]		8	13	5	3	6	3					
22.95°	ω $\{10\bar{1}3\}$	13	34	22	18	13	22	23	22	35	27	11	29
32.42°	π $\{10\bar{1}2\}$	10	9	6	20	10	5	13	17	6	21	21	6
51.79°	r, z $\{10\bar{1}1\}$										6		
90.00°	m $\{10\bar{1}0\}$												
47.73°	ξ $\{11\bar{2}2\}$					3			11		3	5	
65.56°	s $\{11\bar{2}1\}$	3					3	3			3	3	
73.71°	ρ $\{21\bar{3}1\}$				3		3			6	9		
82.07°	x $\{51\bar{6}1\}$												3
90.00°	a $\{11\bar{2}0\}$												
77.20°	$\{22\bar{4}1\}$												3
77.91°	$\{31\bar{4}1\}$						5						3
78.87°	t $\{40\bar{4}1\}$					3							
90.00°	k $\{51\bar{6}0\}$												
17.62°	e $\{10\bar{1}4\}$	28	16	11	18	10	11	23	6	6	3	18	16
Unindexed[a]		13	14	14	5		8	10	11	12	18	8	19

Note: Samples are arranged in order of increasing depth.

[a]Unindexed orientations are those which provide measurements that do not correspond to the rational PDF crystallographic orientations.

[b]PDF planes overlap $\{10\bar{1}4\}$ and $\{10\bar{1}3\}$ crystallographic orientations.

TABLE 3. Crystallographic orientation abundances of PDFs (%) derived from universal stage measurements of shocked quartz grains in breccia dikes in the M4 drill core, Morokweng impact structure.

Rock type		Suevite	Suevite	Pseudotachylite	Pseudotachylite	Pseudotachylite	Suevite
Sample no.		M4 S-7	M4 S-2	M4 A-INJ	M4 IM-2	M4 IM-6	M4 S-5
Depth (m)		146.68	156.35	189.00	234.33	271.17	285.97
Number of investigated grains (n)		5	15	12	10	6	15
Number of measured sets (Q)		6	28	20	14	10	16
Number of PDF sets/grain (Q/n)		1.2	1.9	1.6	1.4	1.6	1.1
Polar angles and PDF crystallographic orientations		Absolute frequency (%)					
0.00°	c (0001)	50	36	40	36	20	44
	$\{10\bar{1}4\}/\{10\bar{1}3\}$[b]	n.d.	4	n.d.	8	n.d.	n.d.
22.95°	ω $\{10\bar{1}3\}$	17	32	20	36	30	25
32.42°	π $\{10\bar{1}2\}$	n.d.	4	20	n.d.	n.d.	6
51.79°	r, z $\{10\bar{1}1\}$	n.d.	n.d.	n.d.	n.d.	n.d.	n.d.
90.00°	m $\{10\bar{1}0\}$	n.d.	n.d.	n.d.	n.d.	n.d.	n.d.
47.73°	ξ $\{11\bar{2}2\}$	n.d.	n.d.	n.d.	n.d.	20	n.d.
65.56°	s $\{11\bar{2}1\}$	17	n.d.	n.d.	n.d.	10	n.d.
73.71°	ρ $\{21\bar{3}1\}$	n.d.	n.d.	n.d.	n.d.	n.d.	n.d.
82.07°	x $\{51\bar{6}1\}$	n.d.	n.d.	n.d.	n.d.	n.d.	n.d.
90.00°	a $\{11\bar{2}0\}$	n.d.	n.d.	n.d.	n.d.	n.d.	n.d.
77.20°	$\{22\bar{4}1\}$	n.d.	n.d.	n.d.	n.d.	n.d.	n.d.
77.91°	$\{31\bar{4}1\}$	n.d.	n.d.	n.d.	n.d.	n.d.	n.d.
78.87°	t $\{40\bar{4}1\}$	n.d.	n.d.	n.d.	n.d.	n.d.	n.d.
90.00°	k $\{51\bar{6}0\}$	n.d.	n.d.	n.d.	n.d.	n.d.	n.d.
17.62°	e $\{10\bar{1}4\}$	17	7	5	14	n.d.	13
Unindexed[a]		n.d.	18	15	7	20	13

Note: Samples are arranged in order of increasing depth.
Abbreviation: n.d.: not detected.
[a]Unindexed orientations are those which provide measurements that do not correspond to the rational PDF crystallographic orientations.
[b]PDF planes overlap $\{10\bar{1}4\}$ and $\{10\bar{1}3\}$ crystallographic orientations.

phyllosilicates, resulting in scalloped fracture margins (Figure 3a,e).

Quartz grains in a few samples display a toasted appearance characterized by gray-brown domains comprising dense arrays of sub-micron-scale inclusions (Figure 3f). Whitehead et al. (2002) attributed these dense concentrations of submicroscopic fluid inclusions to the exsolution of H_2O from shock glass associated with PDF planes during post-shock recrystallization. Toasting may be patchily developed in individual grains in M4 core samples—domain boundaries appear to relate to healed intragranular fractures adjacent to which the submicroscopic features are absent. Localized fracture-remediated diffusion and/or recrystallization of the quartz alongside the fractures, as proposed by Whitehead et al. (2002), may be the cause.

Feldspars

Shock effects that have been reported in feldspars from meteorites and other impact structures include a range of features such as planar fractures and offset twins, alternate twin deformation (e.g., ladder texture; isotropization of alternate albite twins), preferential alteration or toasting/darkening of alternate twin lamellae, patchy or partial isotropization of grains, mosaicism, and/or shock darkening (Engelhardt et al., 1968; French et al., 1997; Harris et al., 2010; Pati et al., 2010; Pickersgill et al., 2013; Rubin, 1992); however, some of these features are indistinguishable from features formed by endogenic processes, and are therefore, equivocal (see review in Pickersgill et al., 2021). Moreover, unlike quartz, feldspar is susceptible to alteration, which may destroy evidence of the origin of impact-related features (Pickersgill et al., 2021).

Plagioclase is present in all the target rocks in the M4 drill core but ranges from albite-oligoclase in the granitoid gneisses and metadolerite to labradorite in the dolerite. Microcline and/or alkali feldspar are present in only some granitoid gneisses (Gibson et al., 2022). Feldspars also occur in lithic clasts or as mineral clasts within the suevite and pseudotachylite dikes. Feldspar grains display a range of non-shock-diagnostic internal deformation features, such as undulose and patchy extinction, kinking or bending of twins in plagioclase, and intragranular planar

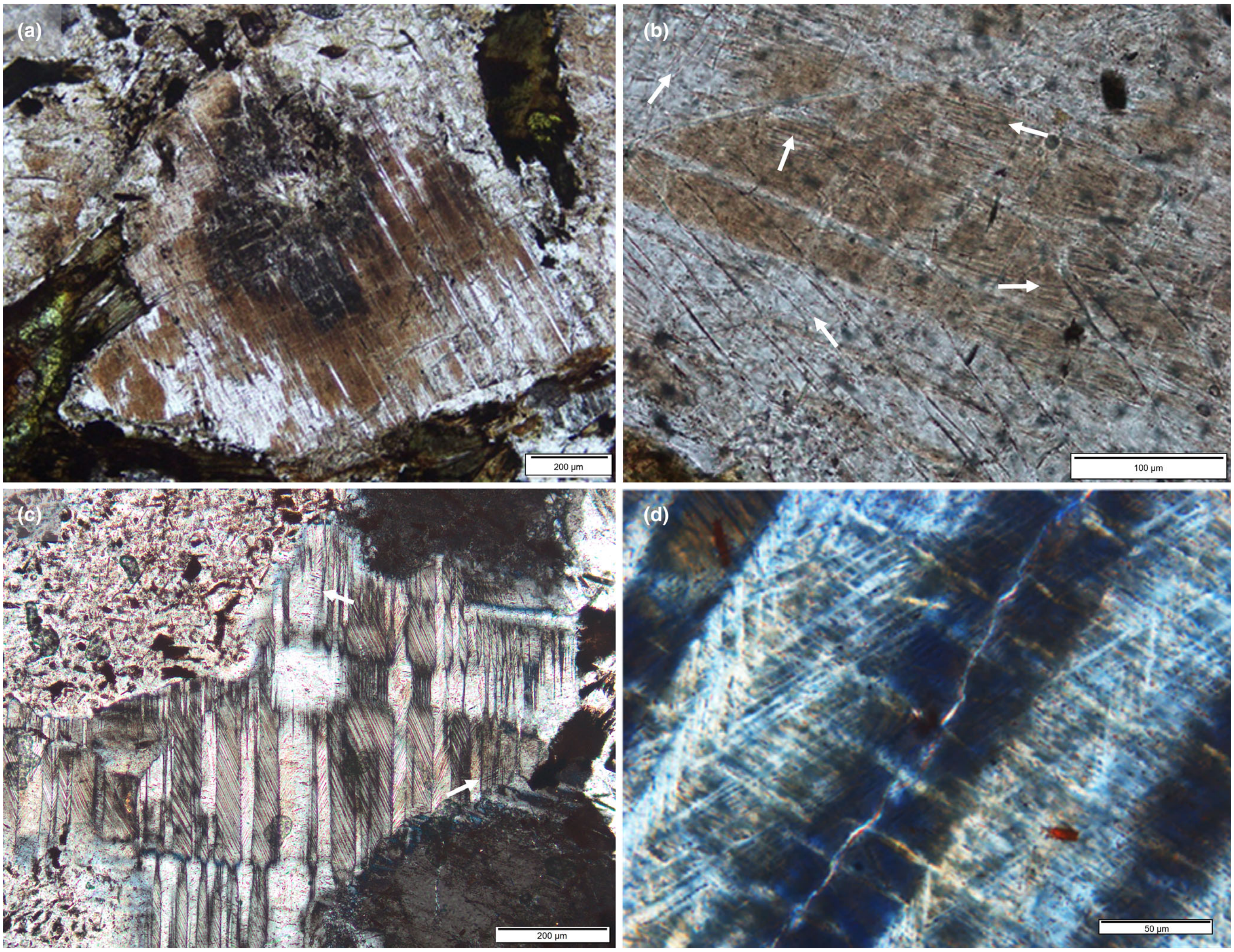

FIGURE 4. Impact-induced features in feldspars in the M4 drill core. (a) Discolored plagioclase core with some alternate twin variability (PPL, sample AM5, 362 m depth). (b) Alternate twin discoloration, multiple sets of planar features (arrows) and closely spaced subplanar fractures in plagioclase (PPL, sample AM5, 362 m depth). (c) Microcline showing original coarse tartan twins overprinted by fine polysynthetic twin lamellae that produce a chevron pattern. Arrows indicate minor additional planar feature sets (partial XPL, sample GG8, 152 m depth). (d) Detail of chevron arrangement of fine twin lamellae in microcline, showing their spindle shape. A third set lies orthogonal to the main twins, parallel to thin perthite exsolution lamellae. The speckled appearance of the twin lamellae relates to microscopic cavities caused by hydrothermal alteration (XPL, sample GG2, 132 m depth). (Color figure can be viewed at wileyonlinelibrary.com)

fractures that offset twin lamellae, which in many cases become more closely spaced toward cataclasite, suggesting they are linked to post-shock faulting. These fractures are typically filled by hydrothermal zeolite and/or phyllosilicate minerals.

Features resembling PDFs, ladder texture, alternate twin deformation, and darkening/toasting are found in both Na-rich plagioclase and microcline in granitoid gneisses the M4 drill core (Figure 4), but are far less common than the PDFs in quartz. The most commonly developed feature in plagioclase comprises 1–5 μm wide, closely spaced (<10 μm), planar to spindle-shaped lamellae that are oriented oblique, to orthogonal, to the main polysynthetic or tartan twin planes (Figure 4). In most cases, these lamellae terminate at the boundaries of larger twins, but in some cases, they do extend across twin planes. The lamellae appear dark even in plane-polarized light (Figure 4b); BSE analysis indicates that they are defined by highly elongated cavities lined by micron-sized aggregates of alteration minerals. The darkening thus appears to be caused by light refraction, rather than an isotropic or opaque phase. Stöffler (1967) noted both isotropic and non-isotropic, low-birefringence, lamellae in plagioclase from the Ries crater, whereas Pickersgill et al. (2015) suggested that similar lamellar features in plagioclase from the Mistastin Lake impact structure represent compositionally distinct lamellae. No evidence of compositionally distinct feldspar phases was found under BSE analysis (whereas (anti-)perthite exsolution is clearly visible, e.g., Figure 4d); however, it is not possible to tell if the differential alteration represents exploitation of microtwin planes by hydrothermal fluids or devitrification-replacement of a shock glass.

Microcline grains locally contain larger spindle-shaped lamellae up to several hundred microns long and a few tens of microns wide that produce a distinctive chevron pattern oblique to the tartan twinning (Figure 4c,d). These lamellae are anisotropic, and are thus, not glass. BSE analysis confirms they are not exsolution features. It is beyond the scope of the present study to establish whether these are shock-induced twins, but their fine-grained nature and apparent restriction to rocks in the MIS suggest an impact link. Darkening and discoloration of the grains in transmitted light thus appear to be a consequence of disruption of light along these discontinuities.

Plagioclase in the granitoid gneisses locally displays pale yellow-gray to dark gray discoloration under PPL in irregular patches (Figure 4a) and/or in alternate twins (Figure 4b). These patches or alternate twins display reduced birefringence relative to the rest of the grain and, under high magnification, appear to be linked to submicroscopic, crystallographically controlled cavities lined with micron-sized phyllosilicates. No evidence was found of submicroscopic Fe droplets similar to those described by Rubin (1992) and Moreau et al. (2017) as the cause of shock darkening in feldspars from chondrites; consequently, refraction caused by the numerous cavities appears to be the most likely cause of darkening in feldspars from the M4 drill core.

Jaret et al. (2014) and Pickersgill et al. (2015) proposed that alternate twin isotropization only occurs at relatively low shock pressures, where subtle crystallographic orientation differences between twin lamellae are capable of producing different strain responses compared with the more uniform response that occurs at higher shock pressures. While Ferrière et al. (2009) suggested that toasting in quartz was related to annealing of glass at high temperature, it seems unlikely that shock pressure and post-shock temperature in the M4 core were sufficiently high to cause this in quartz and feldspars. The evidence of (as yet unconfirmed) PDF-type features in the sodic plagioclase in the granitoid gneiss samples (Figure 4b), but their absence in labradoritic plagioclase in the dolerite samples, could be explained by shock heterogeneity in the core but would also be consistent with more calcic plagioclase requiring a higher shock pressure threshold for formation of shock features (Pickersgill et al., 2021).

No unequivocal evidence of feldspar mosaicism or diaplectic glass was observed, but crystalplastic and brittle strain processes linked to the post-impact faulting, and clouding of grains by hydrothermal alteration complicate textural analysis. Although microcrystalline feldspar aggregates, interpreted as annealed feldspar glasses, have been found associated with feldspar clasts in pseudotachylite (Wela, 2017), their absence in other rock types in the M4 core suggests that these glasses have a frictional, rather than shock, melt origin.

Mafic Minerals

Biotite is present in only small amounts in the granitoid gneisses, except in monzonitic gneiss where it reaches 15 vol% (Gibson et al., 2022). Biotite grains generally contain kink bands (Figure 5a). Given the evidence for both pre-impact and post-shock, impacted-related, deformation in these rocks, the kink bands in biotite grains cannot be unequivocally linked to the shock. Nonetheless, Agarwal et al. (2019) and Ebert et al. (2021) recently demonstrated that shock does produce varying biotite kink band geometries as a function of the differing orientations of grain crystallographic axes relative to the shock propagation direction. As with the polysynthetic twinning in the feldspars, the fineness and intensity of the kinking in biotite grains might provide qualitative support for a shock origin. Likewise, intense kinking of small biotite inclusions in the cores of large plagioclase grains that appear otherwise unaffected by brittle strain might also point to the transfer of a shock pulse through the host grain. Biotite grains are locally preferentially altered to neoblastic ilmenite, titanite and chlorite along kinks and at their margins, which suggests preferential retrograde hydrothermal replacement where the lattice has undergone maximum strain, rather than shock-induced dissociation of biotite to oxide phases, which occurs at >30 GPa (e.g., Ogilvie et al., 2011).

Pyroxene, amphibole, biotite, and chlorite in the dolerite and metadolerite are generally highly altered to fine-grained aggregates and/or disrupted by cataclasis, hence it was not possible to systematically investigate possible grain-scale shock effects in these minerals.

Accessory Minerals

Apatite, zircon, titanite, and epidote are found in all granitoid gneisses in the M4 drill core but are particularly abundant in the monzonitic gneiss (Gibson et al., 2022). All display planar to subplanar features (Figure 5), which may indicate a shock origin; however, this requires further detailed study.

Apatite may display either a single basal or up to two oblique, planar to subplanar fracture sets (Figure 5b) that BSE analysis shows have been annealed (Figure 5d). In some grains, conjugate alignments are suggestive of the shock-induced conjugate fracture sets described by Cox et al. (2020); however, more thorough analysis is needed.

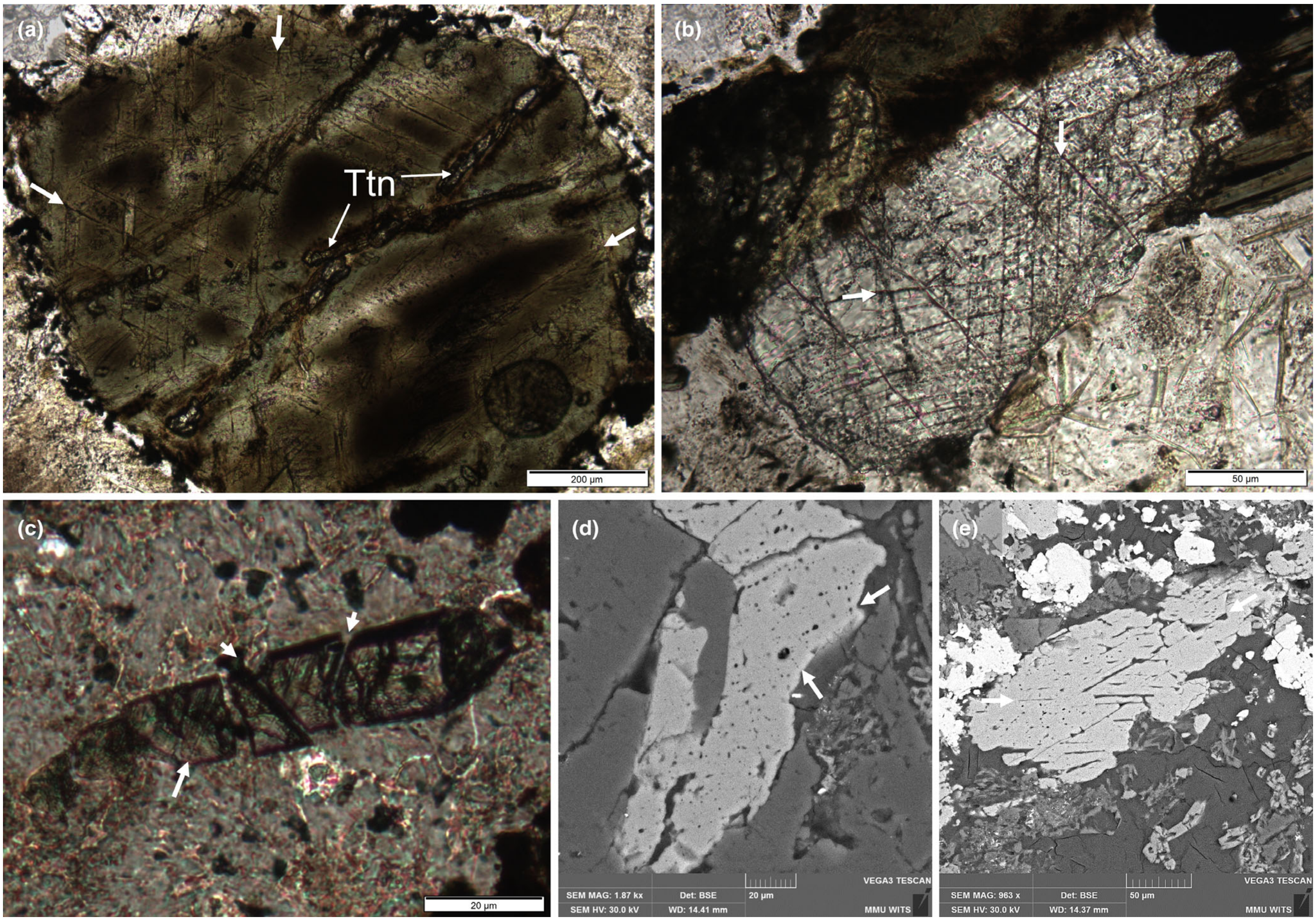

FIGURE 5. Impact-induced features in mafic and accessory minerals in the M4 drill core. (a) Biotite showing multiple fine kink band orientations (arrows), with two prominent orientations replaced by neoblastic hydrothermal titanite (Ttn). The patchy color is linked to variable chloritization along the intersecting kink bands (PPL, sample AM5B, 362 m depth). (b) Intense planar and subplanar fracturing in apatite, with local areas displaying strong crystallographic control. The apparent curvature of the east–west-trending fracture set toward the bottom left is an artifact of different crystal faces (PPL, sample AM5A, 362 m depth). (c) Zircon showing conjugate fractures (short arrows) that preferentially exploit more finely spaced planar features (long arrow indicates the NNE–SSW set) (PPL, sample R22, 139 m depth). (d) SEM BSE image showing two annealed fracture sets in apatite, defined by µm-scale fluid inclusion cavities (sample GG8, 152 m depth). (e) SEM BSE image of titanite showing annealed conjugate fracture cleavage (sample GG10, 165 m depth). (Color figure can be viewed at wileyonlinelibrary.com)

In a geochronological study of the granitoid gneisses, Gibson et al. (2022) noted single or conjugate planar fracture sets in several zircon grains. Figure 5c shows a grain containing planar features oblique to the crystallographic c-axis, some of which were subsequently reactivated by dilational or shear displacements.

Titanite grains locally display conjugate internal planar fractures (Figure 5e). The cleavage resembles shock-activated mineral cleavage seen in amphiboles in the Vredefort Dome (Gibson & Reimold, 2005) but cannot be unequivocally linked to shock. Polysynthetic twinning is found in a few grains, but further detailed analysis is required to establish if it conforms to the specific orientations noted by Timms et al. (2019) as forming under shock pressures of 12–17 GPa.

Primary epidote in the granitoid gneisses commonly displays the most intense in situ fracturing of all the accessory phases; however, sets of subparallel planar fractures are not visible, and extensive phyllosilicate alteration complicates internal textural analysis. No comparative literature on the shock behavior of epidote is available.

Universal Stage Analysis of PDF Crystallographic Orientations in Quartz

The crystallographic orientations of PDFs in quartz are the most commonly used parameter for quantitative shock barometry at low to moderate (~8–25 GPa) shock pressure levels (Ferrière et al., 2009;

French, 1998, and references therein). In samples from the M4 drill core, as in most impact structures, the original thin (1–2 μm) PDF glass lamellae are annealed but remain defined by planar fluid inclusion trails (decorated PDF). Goltrant et al. (1992) and Leroux et al. (1994) showed that fluid inclusion planes also mark shock-induced mechanical basal Brazil twins, which would otherwise be difficult to identify.

Among the 18 samples selected for U-stage analysis, 12 are granitoid gneisses, three are suevites and three are pseudotachylites. Unfortunately, the heterogeneous nature of the M4 core, with significant intervals of quartz-poor doleritic rocks and two significant cataclasite–suevite–pseudotachylite intersections (Gibson et al., 2019; Figure 1b), precluded a uniform sample spacing, such as was more successfully implemented for drill cores from West Clearwater (Rae et al., 2017), Siljan (Holm-Alwmark et al., 2017) and Chicxulub (Feignon et al., 2020) to investigate shock attenuation with depth. The M4 drill core is also significantly shorter than the cores from the other three structures. Likewise, the disrupted nature of major lithological contacts and enhanced alteration in their vicinity precluded investigation of potential shock amplification along any contacts.

Apart from being only an accessory phase in the dolerite, quartz is strongly recrystallized to fine-grained aggregates in the metadolerite samples as a result of greenschist facies metamorphism, which restricted its usefulness for U-stage analysis in this lithology. Even the granitoids may carry fewer than 20 quartz grains in a single thin section owing to the coarse grain size, and the number of grains in the granitoids with PDFs suitable for measuring is further reduced by internal strain, such as undulose extinction, deformation bands, and tiltwalls. Consequently, in each of the 18 samples selected for U-stage analysis, a maximum of only 20 grains per thin section was measured, if possible.

In total, 497 PDF sets in 280 quartz grains were measured, comprising 217 grains (403 sets) from the gneissic target rocks, 35 grains (50 sets) from lithic and mineral clasts in suevite, and 28 grains (44 sets) from clasts in pseudotachylite. The indexed PDF sets are summarized in Tables 2 and 3. For all data sets, absolute frequencies (in %; Engelhardt & Bertsch, 1969; Ferrière et al., 2009; Stöffler & Langenhorst, 1994) are reported. Histograms of absolute frequency percent of indexed PDF sets in quartz for individual samples are presented in Figure 6a,b, and for the cumulative data set in Figure 6c. An average of 1.9 PDF sets per grain was noted across the samples; however, this drops to ~1.5 for the clasts in suevite and pseudotachylite (Table 3). A total of 57 sets (11.5%) are unindexed as they fall outside the accepted 5° margin of error for indexing. A contributing factor may be the internal lattice strain in quartz grains caused by the post-shock, but impact-related, faulting in the M4 drill core; however, a plot of the polar angles of all unindexed sets shows that most lie between 10° and 30° to the *c*-axis (see Supporting Information). This is similar to the pattern seen by Holm-Alwmark et al. (2018) in samples from the Siljan crater, who note that this is a feature of the ANIE methodology that relies for indexing on the angular relationship between rhombohedral planes, rather than the angle between PDF sets and the c-axis.

Tables 2 and 3, and Figure 6, confirm that the PDF orientations in quartz grains in the M4 drill core are dominated by (0001) and $\{10\bar{1}3\}+\{10\bar{1}4\}$. Of the higher-angle sets only the $\{10\bar{1}2\}$ orientation is found consistently, and it constitutes only between 6% and 20% of the measurements. The possible slight increase in the proportion of $\{10\bar{1}3\}+\{10\bar{1}4\}$orientations with increasing depth, and the slightly higher proportions of high-angle PDF sets in the deepest samples (Figure 6), is insufficient grounds to suggest a discernable depth-related trend in shock intensity.

Quartz grains within the suevite dikes occur either as single grains (mineral clasts), as grains within polycrystalline lithic clasts, or as undigested mineral clasts enclosed in melt clasts. Mineral clasts as small as 20 μm show single sets of closely spaced, parallel, planar fluid inclusion trails. The dominant set in all the suevite samples is (0001), with an abundance of >30% in each sample (Table 3); however, it was not possible to obtain as many measurements as for the gneissic wallrocks. Sample M4 S-2 is notably the only suevite sample in which quartz clasts show equivalent abundance of (0001) and $\{10\bar{1}3\}$ orientations (Figure 6b). The $\{10\bar{1}2\}$ set is absent in sample M4 S-7, but this sample is the only suevite with grains recording the $\{11\bar{2}1\}$ set (Table 3, Figure 6b).

The pseudotachylite dikes enclose fewer clasts than the suevites, and these are mostly limited to quartz mineral clasts as a result of more complete melting of the feldspar component in the target rocks (Gibson et al., 2019, 2024). This, together with more intense annealing recrystallization of the quartz clasts and small clast size, limited the number of PDF measurements in these samples, even using multiple thin sections (Table 3). Notwithstanding the restricted number of grains suitable for measurement, the PDF orientation data (Figure 6b) in the pseudotachylite samples are similar to those in both the target rocks and suevites, with (0001) and $\{10\bar{1}3\}$ making up >60% of the combined total. Of the three samples, M4 A-INJ contains quartz clasts that generally display only 1 set (rarely 2 sets are noted), whereas samples M4 IM-2 and IM-6 show a higher proportion of the $\{10\bar{1}3\}$ orientation and an absence of the $\{10\bar{1}2\}$ orientation. Overall, measured PDFs are dominated by orientations of (0001), $\{10\bar{1}3\}+\{10\bar{1}4\}$ and $\{10\bar{1}2\}$, with relative abundances of 33%, 41%, and 10%, respectively (Figure 6c).

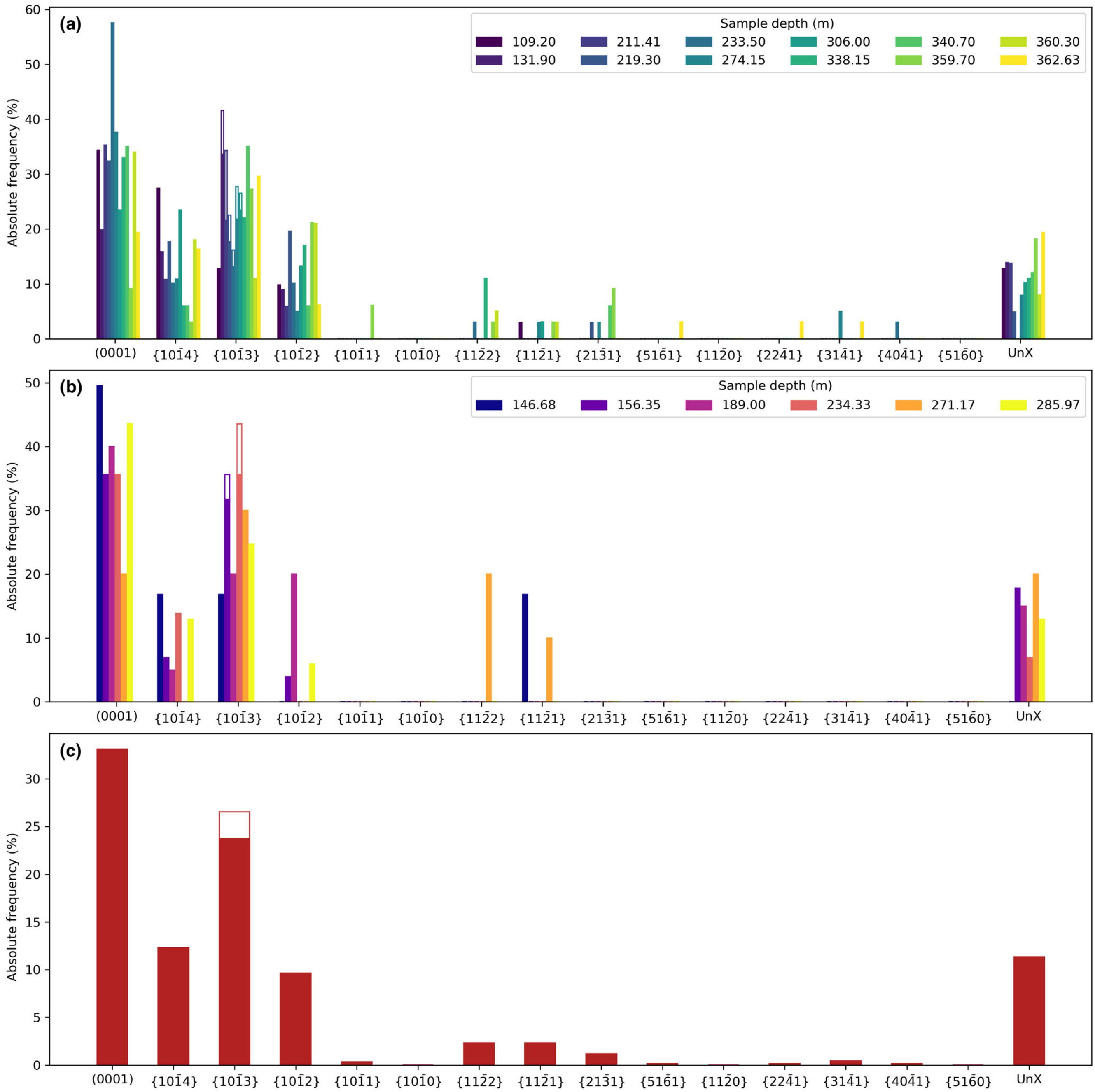

FIGURE 6. Histograms showing the absolute frequencies of PDF orientations (Miller–Bravais indices) for samples from the M4 drill core. UnX, unindexed. (a) Detailed histogram for individual granitoid gneiss samples, in order of increasing depth (darkest to lightest) from left to right. (b) Detailed histogram for individual suevite and pseudotachylite samples, in order of increasing depth (darkest to lightest) from left to right. (c) Histogram showing a compilation of all measurements. See Tables 2 and 3 for data. (Color figure can be viewed at wileyonlinelibrary.com)

Numerical Modeling

The iSALE shock physics code has previously been applied to the Morokweng impact by Potter and Collins (2013), specifically to investigate the unusually high meteoritic component in the impact melt (2%–5%; Koeberl et al., 1997; McDonald et al., 2001) and the survival of meteorite fragments in the melt sheet (Maier et al., 2006). Potter and Collins (2013) modeled only the contact and compression stage of the impact and limited themselves to investigating a range of parameters that would favor impactor survivability and a high meteoritic contribution in the impact melt. Apart from demonstrating how impactor porosity and non-sphericity can play significant roles, they supported McDonald et al.'s (2001) suggestion, based on the general impact modeling of Pierazzo and Melosh (2000), that optimal conditions for these features within the Morokweng impact melt would have been created by a low-velocity and/or high-angle impact, but they did not interrogate other aspects of the model.

In this section, iSALE modeling of the Morokweng impact is extended to include the evolution of the target crust during the excavation and modification stages of cratering to constrain the crater diameter using the new lithological and shock petrographic evidence from the M4 drill core. Specifically, this evaluates the conditions under which structurally elevated, moderately shocked, and strongly faulted crater floor rocks can occur at a radial distance (R) of ~18 km from the center of the Morokweng geophysical anomaly. For the purposes of this first-order analysis, McDonald et al.'s (2001) suggestions of a low-velocity and high-angle impact are adopted.

Table 1 shows the input parameters used in the various simulations. The impact velocity selected for the simulations—11.2 km s^{-1}—corresponds to Earth's escape velocity and is, thus, an absolute minimum to produce a terrestrial impact crater (the currently recognized average impact velocity is 20.5 km s^{-1}; LeFeuvre & Wieczorek, 2011). Using a slow impact velocity produces the most conservative impact melt volume estimates and increases the computational efficiency of the simulation as it reduces the volume of vaporized rock (Pierazzo & Melosh, 2000). The use of the iSALE-2D shock physics code limits these simulations to vertical impacts, but transient crater dimensions are not sensitive to impact angles that exceed 45° (Davison & Collins, 2022). As the target rock sequence in the M4 drill core is similar to that in the M0077A Chicxulub drill core (a mix of mostly granitoid lithologies with subsidiary mafic dikes; for example, Riller et al., 2018), we selected the same acoustic fluidization parameters (γ_η and γ_β; Table 1) as those used in previous simulations of the Chicxulub impact (Rae et al., 2019). Given that both viscosity and decay time scale with impactor diameter, and that impactor diameter can be used as a proxy for crater size, we maintained constant γ_η and γ_β across the different size simulations (see Wünnemann and Ivanov (2003) and Rae et al. (2017) for an explicit explanation) to ensure that viscosity and decay time varied with crater diameter.

Figures 7–10 present different perspectives of the results of five 2D simulations involving respective impactor diameters of 4.2, 6.3, 8.4, 10.5, and 12.6 km, all involving a velocity of 11.2 km s^{-1} and a vertical angle of impact. The craters produced in the 5 simulations have respective final rim-to-rim diameters of ~45, 65, 80, 100, and 120 km. All five simulations predict that impacts in this range would produce a volume of moderately to highly shocked parautochthonous crater basement that would have undergone upward and outward translation during the modification stage of cratering (left side of each image in Figure 7). Peak shock pressure within this displaced volume attenuates with increasing depth (right side of each image in Figures 7 and 9).

The mass of impact melt predicted in each of the simulations tested in Figure 7 is shown in Table 4. In iSALE, this mass corresponds to the region of the target that experiences shock pressure ≥60 GPa, determined from Lagrangian tracer particles. The average density of Morokweng impact melt rock (2647 kg m^{-3}; Henkel et al., 2002) has been used to convert this mass into volume (Table 4, Figure 10). The volume of the impact melt sheet that remains in the crater in each simulation was obtained by subtracting the volume of all the ≥60 GPa tracer particles ejected beyond the final crater rim.

DISCUSSION

Shock Barometry in the Morokweng Impact Structure

Previous Studies

Although several studies have previously reported shock metamorphic features in rocks associated with the MIS (Table 5), some of these features appear ambiguous or could not be unequivocally confirmed owing to extensive annealing/recrystallization; furthermore, quantitative shock barometric studies have been of limited scope. Prior to the present study, only 49 measurements of PDFs in quartz grains, from three geographically dispersed samples, had been performed, and two of these samples were clearly allochthonous, having been modified and transported by post-impact fluvial processes (Corner et al., 1997; Hart et al., 1997; Table 5). The third sample, described by Corner et al. (1997) as a "fragmental breccia of banded ironstone" (p. 359), and by Reimold et al. (1999) as a "parautochthonous breccia" (p. 85), is not sufficiently well-described to establish its significance. A subsequent visit to the site by one of our group (M.A.) identified a breccia of hydrothermal origin, samples of which did not reveal any petrographic evidence of shocked quartz grains. Both the significant elevation of the sample site above the eroded MIS remnant and its location 47 km west of the center of the MIS, present a challenge in the context of more recent studies (see below).

Reimold et al. (2002) described "angular to rounded glass fragments" (p. 223) and "two quartz fragments with one set of PDFs" (p. 224) in a 10 cm wide polymict breccia at a depth of 889 m in the KHK-1 borehole ($R = 40$ km; Figure 1a). No supporting photographic or analytical evidence of the PDFs or glass fragments was

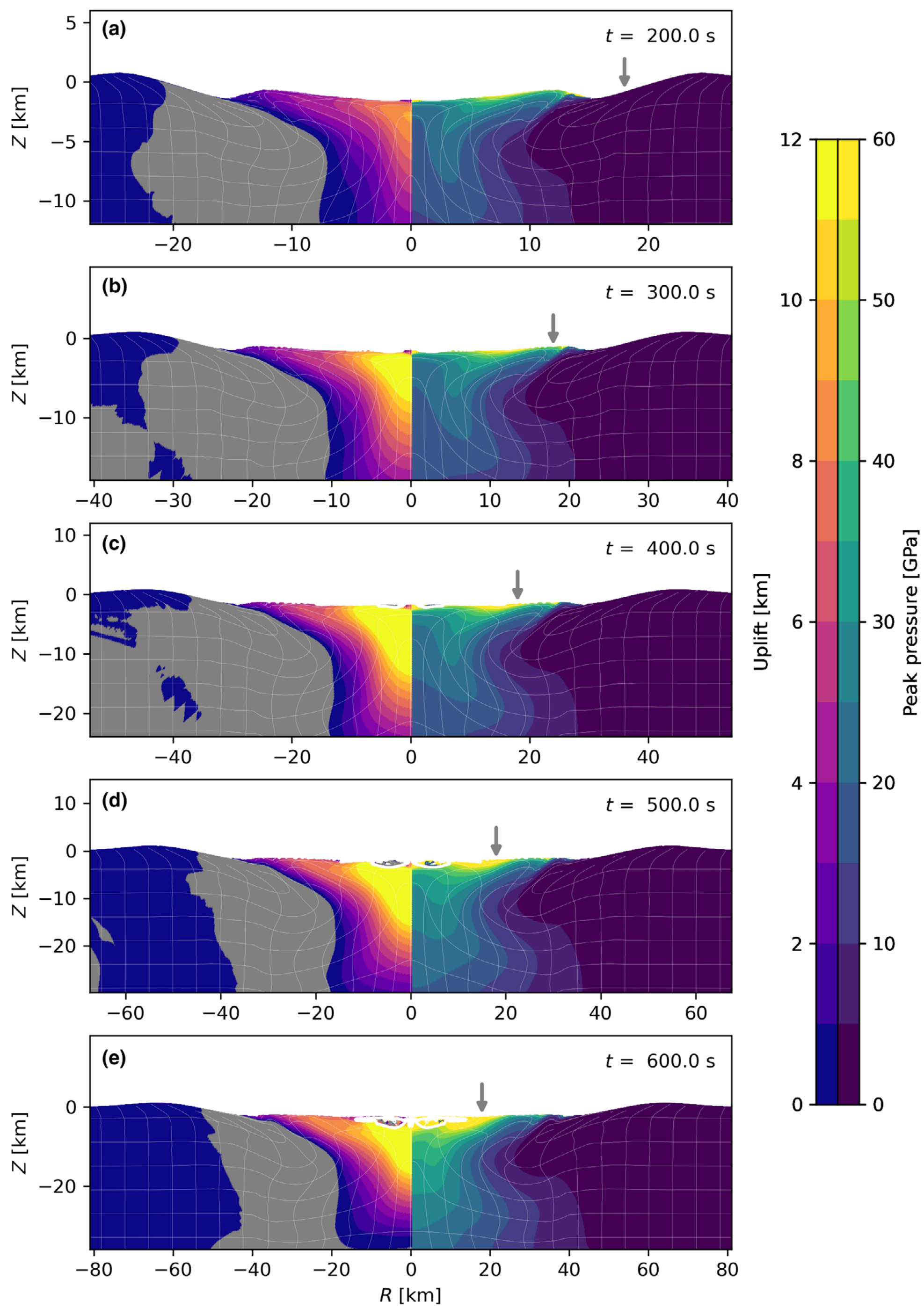

FIGURE 7. Results of iSALE simulations for vertical, $11.2\,\mathrm{km\,s^{-1}}$ impacts of an impactor with respective diameters of (a) 4.2 km, (b) 6.3 km, (c) 8.4 km, (d) 10.5 km, and (e) 12.6 km that produce respective final crater diameters of 45, 65, 80, 100 and 120 km. Left side of each image shows the amount of uplift; right side shows shock pressure distribution following the modification stage. Gray arrow indicates $R = 18$ km. (Color figure can be viewed at wileyonlinelibrary.com)

supplied, but an interpretation of the dike as a suevite was used to derive a diameter estimate for the MIS (see discussion below).

Hart et al. (1997) were only able to obtain PDF measurements in quartz in the WF05 drill core ($R = 6$ km; Figure 1a) from a granite pebble in the basal conglomerate of the Kalahari Group, as attempts to index PDFs in quartz grains in the ~50 m-wide granite intersection toward the base of the hole (Figure 1b) were unsuccessful owing to extensive annealing/recrystallization attributed to the

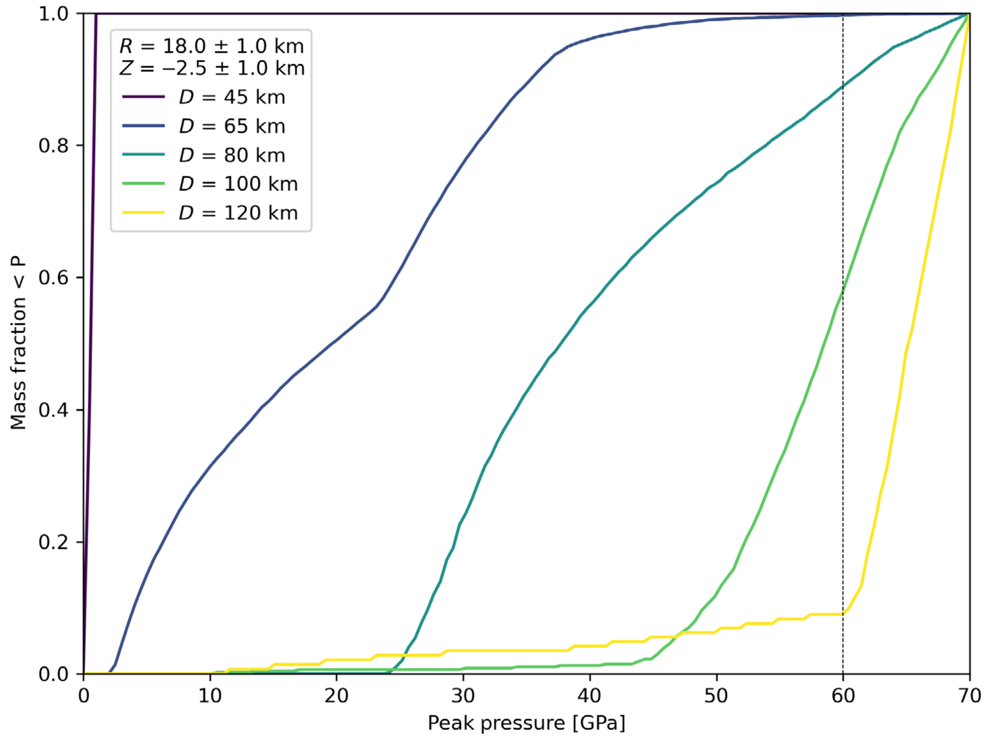

FIGURE 8. Cumulative frequency plot of shock pressure for a 2 × 2 km block centered at coordinates $R = 18$ km, $Z = 2.5$ km for each simulation in Figure 7. Dashed line (60 GPa) corresponds to onset of bulk rock melting. (Color figure can be viewed at wileyonlinelibrary.com)

impact melt sheet (Hart et al., 1997; Reimold et al., 1999). The prevalence of high-angle PDF orientations such as $\{51\bar{6}1\}$ and $\{10\bar{1}0\}$, which together constitute 37% of the total, with $\{10\bar{1}3\}$ also significant (30%) and (0001) constituting only 7% (Hart et al., 1997; Table 5), suggests this sample experienced higher shock pressures than the rocks in the M4 drill core. However, given its central location in the MIS and the fact that it overlies the partially eroded melt sheet (Figure 1a), this pebble is most likely sourced from a clast from the now-eroded upper melt sheet or overlying crater fill breccias, rather than from (par) autochthonous crater basement.

Shock Barometry in the M4 Drill Core

The consistent steep orientation of the foliation and gneissose layering in the granitoid gneisses throughout the M4 drill core (Gibson et al., 2022) favors them representing (par)autochthonous crater basement, rather than a megabreccia. Consequently, the M4 drill core data constitute the first systematic study of shock features in samples from the crater basement of the MIS, and the only unambiguous, in situ, georeferenced, shock barometry estimates for the MIS.

The presence of decorated PDFs in quartz in the M4 lithologies indicates that they experienced shock pressures of at least 5–8 GPa (Hörz, 1968; Stöffler, 1972; Stöffler & Langenhorst, 1994). If the planar features observed in plagioclase in the M4 drill core are shock-induced PDFs then, according to Stöffler et al. (1991), they would signify shock pressures above 15–20 GPa; however, Singleton et al. (2011) suggested that the threshold for their development may be as low as 10 GPa. Jaret et al. (2018) suggested that shock darkening in sodic plagioclase occurs at >24 GPa; however, the optical darkening of some plagioclase and microcline grains in the M4 drill core appears to be related to alteration and, thus, cannot be used as a shock barometer. The observed alternating twin discoloration in the plagioclase (Figure 4a,b) is also consistent with shock pressures of <20 GPa (Jaret et al., 2014), which fits the results of the quartz PDF barometry discussed below.

Shock experiments have confirmed that PDFs in mineral grains become more abundant and more closely spaced with increasing shock pressure (e.g., Dressler et al., 1998; Feldman, 1994; Feldman et al., 1996; Ferrière et al., 2008; Grieve & Robertson, 1976), although distributions are seldom uniform at a grain scale (e.g., Figure 3a). With a few caveats, this allows the orientations and proportions of PDFs in quartz from experiments to be used to calibrate the peak shock pressure attained in natural samples. The (0001) orientation is the indicator of the lowest shock pressures,

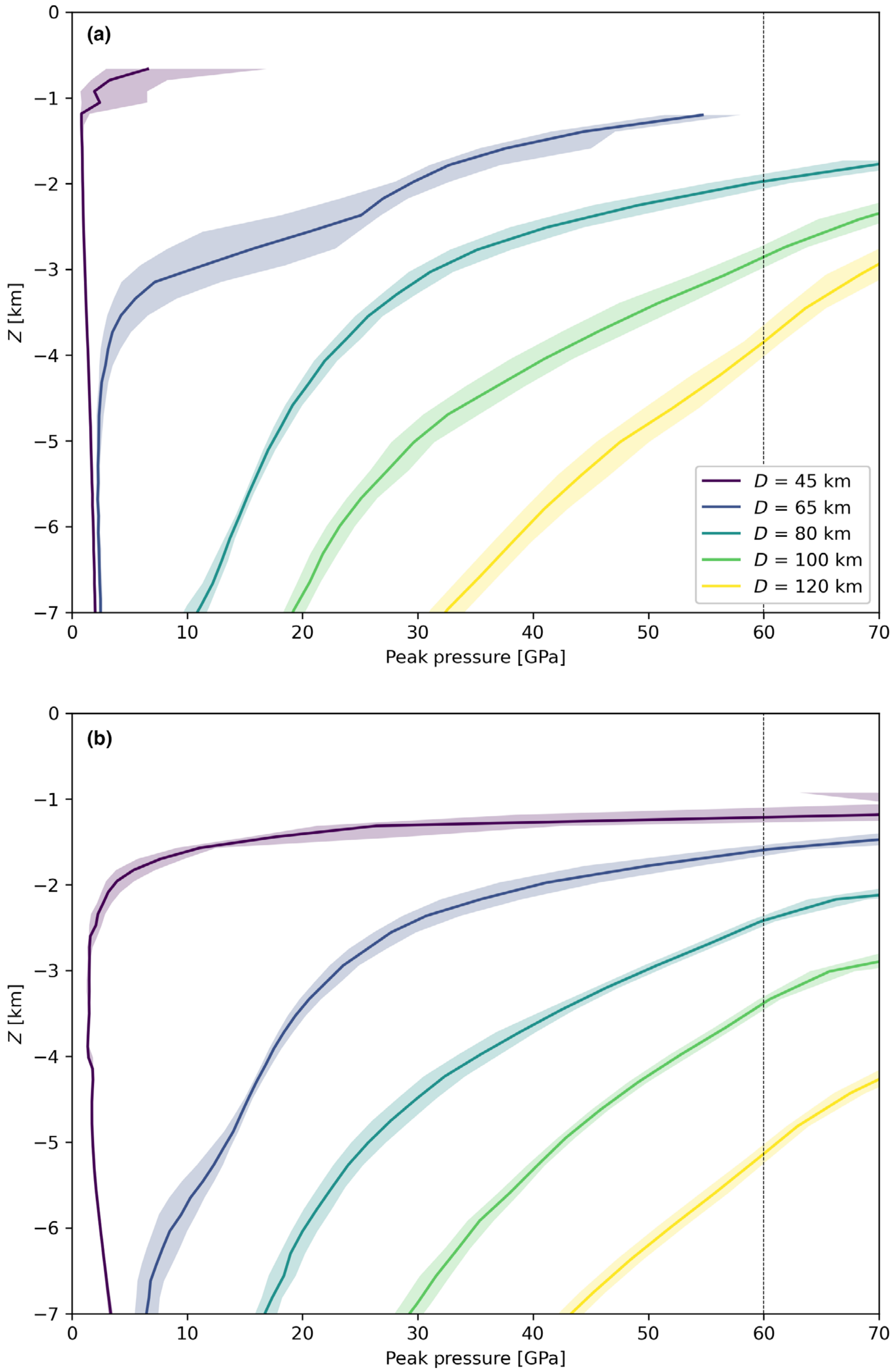

FIGURE 9. Attenuation of median peak shock pressure as a function of depth (Z) based on the iSALE modeling of 5 vertical, low-velocity, impacts shown in Figure 7, for (a) $R = 18$ km, corresponding to the M4 borehole location, and (b) $R = 14$ km, corresponding to the M3 borehole location (Figure 1a). Dashed line (60 GPa) corresponds to onset of bulk rock melting. Error bars reflect the interquartile range of peak pressures within ± 1 km radial distance of the M4 and M3 locations. Comparison of (a) with Figure 8 shows that small changes of a few hundred meters in the selected depth range of the 2×2 km reference block, or a few km in R produce significant changes in the cumulative shock P estimates. The actual distribution is additionally dependent on, inter alia, the kinematic viscosity used in the modeling and whether large-scale fault block displacements occur following the shock compression stage. (Color figure can be viewed at wileyonlinelibrary.com)

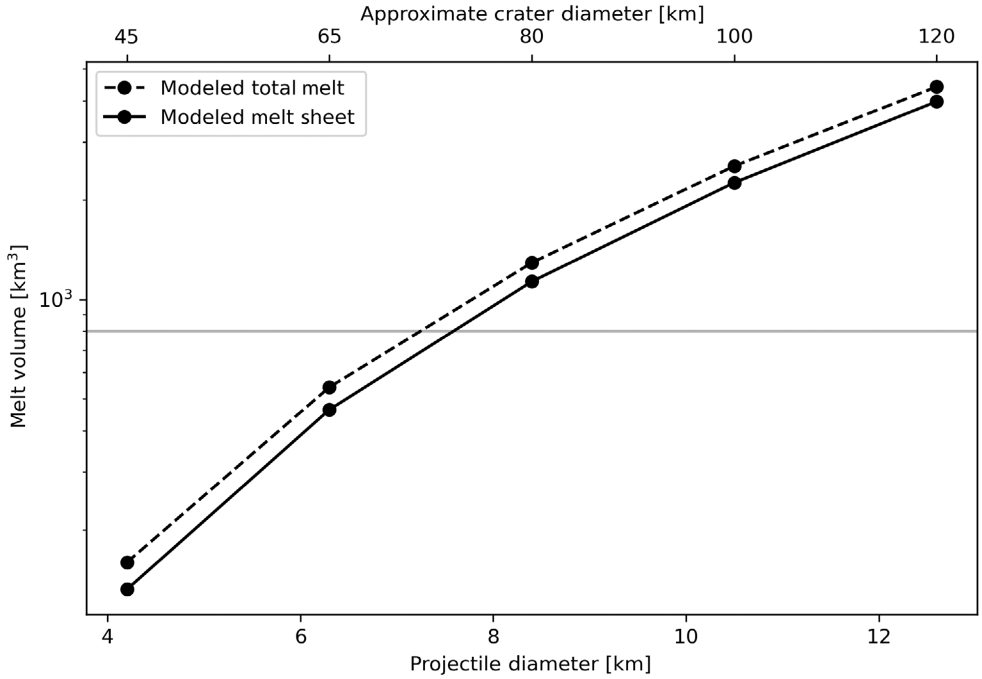

FIGURE 10. Crystalline impact melt volume based on the iSALE modeling of five vertical, low-velocity, impacts shown in Figure 7. Data are shown in Table 4. The gray line indicates the melt sheet volume calculated by Kenny et al. (2021).

TABLE 4. Melt volumes from iSALE-2D simulations for 45, 65, 80, 100, and 120 km final crater diameters (see Figure 7).

Projectile diameter [km]	Projectile velocity [km s^{-1}]	Final crater diameter [km]	Melt mass total [kg]	Melt mass retained [kg]	Melt volume total [km^3]	Melt volume retained [km^3]
4.2	11.2	45	4.22×10^{14}	3.49×10^{14}	159.3	131.9
6.3	11.2	65	1.43×10^{15}	1.23×10^{15}	541.4	462.8
8.4	11.2	80	3.42×10^{15}	3.00×10^{15}	1291.3	1132.2
10.5	11.2	100	6.72×10^{15}	5.98×10^{15}	2536.8	2259.2
12.6	11.2	120	1.17×10^{16}	1.05×10^{16}	4412.5	3981.9

Note: Volume conversions are based on a final melt rock density of 2647 kg m^{-3} (Henkel et al., 2002); the retained mass/volume increases from 82% to 90% of original values with increasing crater size, owing to less efficient crater excavation in the larger craters (Holsapple, 1993).

and with increasing pressure, respectively, $\{10\bar{1}3\}$ and $\{10\bar{1}2\}$ orientations become increasingly dominant at its expense. The $\{10\bar{1}3\}$ orientation appears to form at 12–15 GPa to >16 GPa (French, 1998; Grieve et al., 1996). At >22 GPa, the prevalence of the $\{10\bar{1}2\}$ set appears to equal or exceed $\{10\bar{1}3\}$ (Engelhardt & Bertsch, 1969; Grieve et al., 1996; Hörz, 1968). Stöffler and Langenhorst (1994) suggested that the $\{10\bar{1}3\}$ and $\{10\bar{1}2\}$ orientations are typical of peak shock pressures of ~20 GPa when occurring together with other sets. Rae et al. (2017) proposed that quartz dominated by the $\{10\bar{1}3\}$ set reflects shock pressures of 10–20 GPa. In the M4 drill core samples, the preponderance of (0001), $\{10\bar{1}3\}$ and $\{10\bar{1}2\}$ PDF orientations, with the $\{10\bar{1}3\}$+$\{10\bar{1}4\}$ set constituting 41% of measurements, the (0001) set 33%, and the $\{10\bar{1}2\}$ set contributing 10% (rarely 20%; Tables 2 and 3, Figure 6c), suggests that the target rocks experienced an overall peak shock pressure most likely not higher than ~15–16 GPa (see, e.g., Holm-Alwmark et al., 2018; Rae et al., 2017, 2019).

Several studies have also used the average number of PDF sets per grain in a sample as a proxy for shock pressure, although it must be noted that these estimates are entirely dependent on the accuracy of the calibration scheme selected. Ferrière et al. (2008) and Rae et al. (2019) suggested that an average of 1.5 sets per grain would be consistent with a shock pressure of ~15 GPa, whereas Ferrière et al. (2008) proposed that an average of two sets per grain implies a shock pressure of >16 GPa in non-porous crystalline materials. The

TABLE 5. Previous shock metamorphism and shock barometry studies in the Morokweng impact structure.

Reference	Geological context	Shock feature	Photographic evidence	PDF indices, statistics	Shock P (GPa)	Comment
Corner et al. (1997)	"Fragmental breccia of banded ironstone," $R \sim 47$ km	Decorated PDF in quartz	Yes	Up to 5 PDF sets per grain, but only max. 3 sets could be indexed; <0.01% of grains shocked; 22 measurements from 18 grains combined across both samples; 2 grains showing 2 sets and 1 grain 3 sets: (0001) 9%, $\{10\bar{1}3\}$ 9%, $\{11\bar{2}1\}$ 9%, $\{2\bar{1}\bar{3}1\}$ 18%, $\{10\bar{1}2\}$ 14%, $\{10\bar{1}1\}$ 14%, $\{11\bar{2}2\}$ 5%, $\{51\bar{6}1\}$ 5%, unindexed 18%	12–16	Combination of measurements from 2 samples is problematic. Subsequent site visit by M.A.G. Andreoli) identified breccia as hydrothermal and failed to identify PDF in other samples
	Black Reef Formation (quartzite) boulder $R \sim 75$ km	Decorated PDF in quartz	Yes			Combination of measurements from 2 samples is problematic. Allochthonous boulder, therefore exact provenance within MIS unknown
Hart et al. (1997)	Granite pebble in Kalahari Group basal conglomerate, WF05 drill core (112 m), $R = 7$ km	Decorated PDF in quartz	Yes	27 planes in 21 quartz grains; mostly single sets but 2 sets in 6 grains: $\{10\bar{1}3\}$ (30%), $\{51\bar{6}1\}$ (22%), $\{10\bar{1}0\}$ (15%), $\{2\bar{1}\bar{3}1\}$ (11%), (0001) (7%), $\{10\bar{1}2\}$ (7%), unindexed 7%	10–25	Allochthonous; most likely clast from impact melt
	Brecciated granite gneiss, WF05 drill core (225–271 m), $R = 7$ km	Decorated PDF in quartz	Yes	Up to 3 sets per grain	N/A	Tentatively interpreted as autochthonous basement; too recrystallized to index PDF
Andreoli et al. (1999)	Brecciated granite gneiss, WF05 drill core (225–271 m), $R = 7$ km	Plagioclase mosaicism, PF, PDF and spherulitic pseudomorphs after possible plagioclase glass/melt	Yes (PDF, PF in plagioclase)	N/A	N/A	Too recrystallized to confirm origin of glass/melt
Reimold et al. (1999)	Brecciated granite gneiss, WF05 drill core (225–271 m), $R = 7$ km	Decorated PDF in quartz; PDF in plagioclase and K-feldspar; diaplectic quartz glass, ballen quartz, possible shock melts (annealed)	Yes (PDF in quartz, K-feldspar)	2–3 sets per quartz grain	N/A	Reinterpreted as breccia zone; too recrystallized to index PDF and confirm origin of melts
Reimold et al. (2002)	10 cm "suevite dike," KHK-1 drill core (889 m), $R = 40$ km	Decorated PDF in quartz; rounded glass fragments	No	1 set each in 2 grains; unindexed	N/A	No photographic proof of PDF or glass

average of 1.9 sets per grain for the entire M4 data set (Tables 2 and 3) would thus be consistent with a shock pressure of ≤16 GPa.

As shock pressure attenuates radially in the target crust during an impact (Melosh, 1989), the moderately high shock pressure estimates obtained from the M4 drill core samples require that the M4 rock volume must have lain close to the original transient crater wall (e.g., Figure 11a). This rules out the possibility that the M4 rocks formed part of a large allochthonous basement block from the upper crater wall that slumped inwards to its current position during the modification stage of cratering.

Figures 7, 9, and 11 show that such shallow parautochthonous crater basement located a significant distance from the crater center should show shock pressure attenuation with increasing depth. In recent years, evidence of such shock attenuation has been described in parautochthonous crater basement from long drill cores from the Siljan (Holm-Alwmark et al., 2017) and West Clearwater (Rae et al., 2017) craters. At Chicxulub, Feignon et al. (2020) obtained relatively constant peak shock pressure estimates of 16–18 GPa through the upper ~300 m of the crater basement intersected in the M0077A drill core but suggested that a slight drop to 15–16 GPa may be evident below this. No conclusive evidence of attenuation with depth was noted in the M4 drill core. This could reflect the limited core length (272 m) through the basement succession (Figure 1b); however, the core also shows evidence of extensive hydrothermal alteration (Wela, 2017). Grieve et al. (1990, 1996) proposed that the underestimation of shock pressures from PDF statistics in quartz in gneisses in the core of the Vredefort Dome could be the result of selective annealing of more delicate, high-angle, PDF sets. Enhanced dynamic, thermal, and hydrothermal (re)crystallization effects in the suevitic and pseudotachylitic breccia dikes in the M4 drill core (Wela, 2017) might similarly explain the lack of observed high-angle PDF sets and lower average number of sets per grain (~1.5, vs. 1.9; Table 3) in clasts in the breccias relative to the wallrock gneisses (Figure 6). However, other factors such as comminution in these fault-hosted breccias may also exert some influence. This lack of evidence of higher peak shock pressure in clasts from the suevite dikes relative to the wallrocks also fits the interpretation that the suevite formed by fault-related processes during the excavation and/or modification stages of cratering, rather than by more conventional mechanisms attributed to suevite genesis (Gibson et al., 2019, 2024; Wela, 2017). Local variations in the extent of hydrothermal alteration might also then explain the highly variable PDF statistics obtained in some cases between adjacent wallrock samples (e.g., M4 AM-4, M4 GG-16; Table 2), although Feignon et al. (2020) proposed that proximity to lithological contacts might also cause such variability.

The evidence of a strong hydrothermal overprint raises the possibility that peak shock pressures obtained from PDF statistics for the M4 drill core as a whole may also be underestimated. Nonetheless, factoring in the deep level of erosion of the MIS (see below), the peak values obtained for the M4 drill core are only slightly lower than the 17–18 GPa peak shock pressure estimates obtained from cores drilled at intermediate distances between the crater centers and rims of the Chicxulub (Feignon et al., 2020) and West Clearwater (Rae et al., 2017) craters, and similar to, or even slightly greater than, those obtained from surface and core samples from equivalent distances in the Manicouagan (Dressler, 1970; Murtaugh, 1976), Siljan (Holm-Alwmark et al., 2017) and Slate Islands (Robertson & Grieve, 1977) structures. The implications of this for constraining the size of the MIS are discussed in the next section.

Crater Morphology and Size

Previous Size Estimates of the MIS

The buried nature of the MIS means that previous estimates of its diameter have been based primarily on interpretation of geophysical data, empirical evidence from small rock chip samples of the sub-Kalahari Group basement rocks recovered from percussion-drilled groundwater and mineral exploration boreholes, and interpolation of regional surface mapping that suggests an arcuate deflection of the shallowly W-dipping Paleoproterozoic supracrustal rocks beneath the Kalahari Group around the western edge of the geophysical anomaly (e.g., Corner et al., 1997; Reimold et al., 1999, 2002, figure 1). Apart from the central magnetic high and the annulus of disrupted magnetic signals, which have a combined radius (R) of ~35 km, Corner et al. (1997) and Andreoli et al. (2007, 2008) suggested that two further crescentic geophysical anomalies, at $R \sim 120$ km and $R \sim 170$ km, might also be related to the impact, which led them to propose significantly larger diameter estimates for the MIS of between 240 and 340 km. Reimold et al. (1999) suggested that the 70-km-wide central geophysical anomaly may represent only the central peak of a ≥200 km diameter crater.

Based on modeling of the magnetic and gravity data, Henkel et al. (2002) proposed a 65–70 km apparent crater diameter and that impact-induced structural uplift of the central crater basement amounted to ~4 km. Reimold et al. (2002) cited the "suevite" breccia dike in the KHK-1 drill core as evidence that the core intersects the rim of the MIS (Figure 1a), and thus, that the MIS has a present (apparent) diameter of 75–80 km. Andreoli et al. (1999) and Hart et al. (2002) suggested three concentric rings (I–III in Figure 1a) corresponding, respectively, to the limits of the melt sheet ($R = 15$ km), "suevite melt breccia"

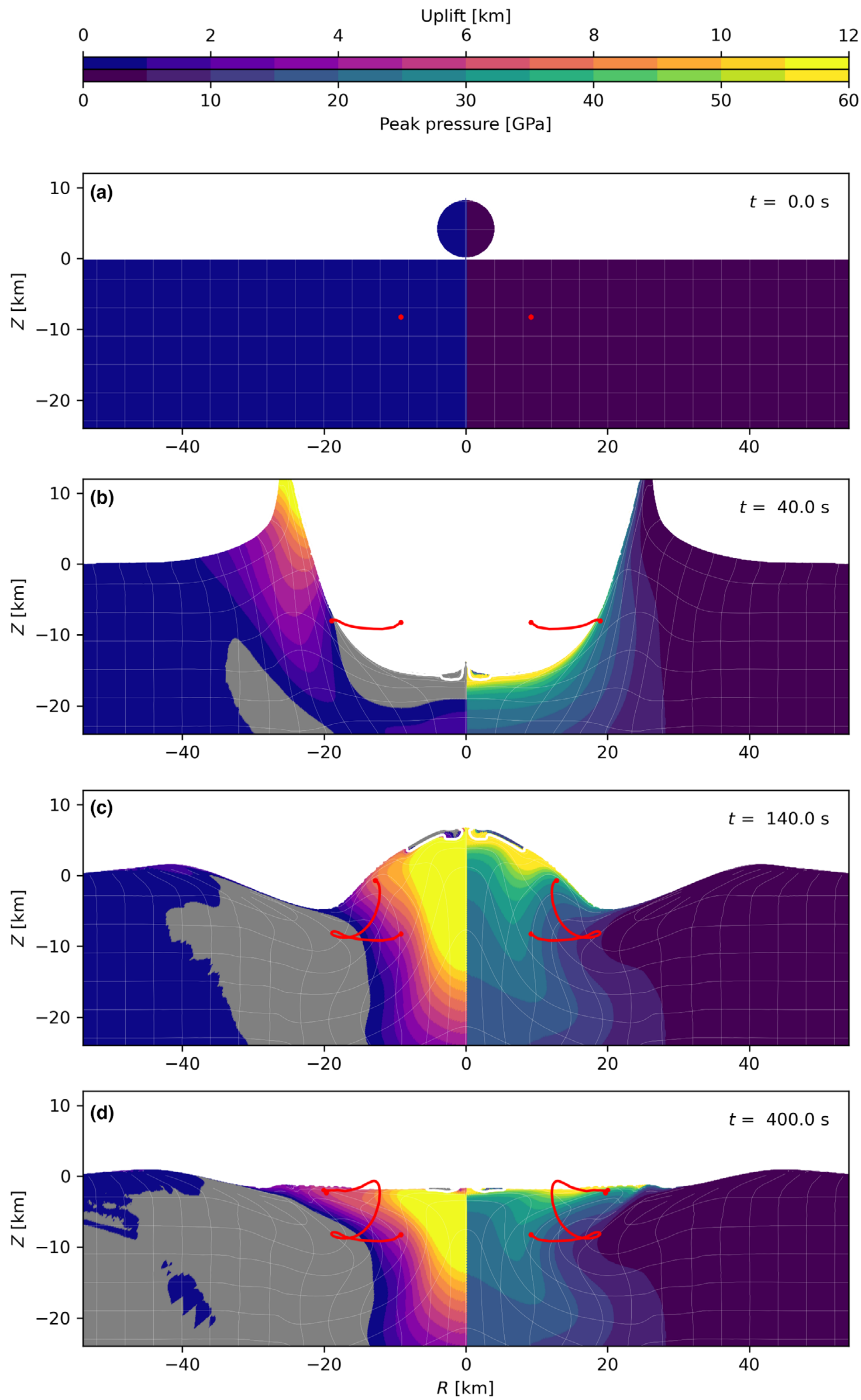

FIGURE 11. Modeled particle trajectory from iSALE for the rock volume intersected in the M4 drill core for an 80 km final crater diameter solution (Figure 7c). See Video S1. (Color figure can be viewed at wileyonlinelibrary.com)

($R = 35$ km) and "brecciated and fractured basement" ($R = 40$ km). The reference to "suevite melt breccia" arises from De Beers Exploration internal company reports that document altered "impact breccia" intersected in a few percussion boreholes drilled between 24 and 29 km ENE to NE of the MIS center as part of a larger regional kimberlite exploration program (A. Macdonald, pers. comm., 2023). Preliminary petrographic analysis of samples of these breccias recently acquired by our group confirms the presence of PDFs in quartz clasts and fluidal-textured particles that may represent altered melt clasts. The allochthonous nature of these breccias is indicated by the absence of any shock-diagnostic features in granite and dolerite intersections in the other holes, which are interpreted as crater basement.

Andreoli et al. (1999) and Hart et al. (2002) present no description of "brecciated and fractured basement" samples corresponding to Ring III, but Henkel et al. (2002) argued that the disrupted magnetic signals that define the outer annulus ($R \sim 15$–35 km) are consistent with large-scale block faulting. Reimold et al. (1999) proposed that a 300 m thick intersection of Paleozoic Dwyka Group diamictite in hydrogeological boreholes at $R \sim 35$ km in the NE sector of the MIS (Smit, 1977) fits the existence of a large listric normal fault with a throw of hundreds of meters linked to crater collapse. More recently, Westgate et al. (2021) suggested that the unusual fault pattern observed in the KBF03A seismic profile ESE of the KHK-1 site and ~ 40 km south of the center of the MIS (Figure 1a) could represent a near-tangential section through an array of concentric faults with large, centripetally directed, normal slip displacements lying near the MIS crater rim.

In summary, the combined geophysical and borehole data suggest a partially eroded structure with a minimum current diameter of between 65 and 80 km and a complex internal morphology that is dominated by a central melt pool and an annulus of fractured and faulted basement which is locally overlain by patches of allochthonous, probably suevitic, impact breccia. Normal faults with significant centripetal displacements appear to lie toward the edge of the structure.

Complex Crater Morphology

The large, and growing, morphometric database for terrestrial and extraterrestrial hypervelocity impact craters confirms that generally well-constrained scaling relationships exist between key morphological parameters and the final rim-to-rim crater diameter (D; e.g., Grieve & Cintala, 1997; Pike, 1985; Wood & Head, 1976). However, caution is required when these morphometric relationships are applied to terrestrial craters as most are modified by post-impact erosional and/or burial processes (Kenkmann, 2021; Turtle et al., 2005).

On Earth, the transition from simple, bowl-shaped, craters to craters with a complex internal morphology occurs at $D = 3$–4 km (Grieve, 1991). Key to understanding why complex craters display different morphologies is the elevation of the central crater basement volume, which rises as it decompresses following the passage of the shock wave. Both the diameter of this centrally uplifted volume and the magnitude of its rise are directly proportional to impact energy, of which crater size is a proxy. Thus, small complex craters ($D < 25$ km) on Earth show a central peak of uplifted basement with a diameter of ~0.22D (Pike, 1985). However, in larger craters, the central uplift over-steepens and collapses outwards as it overrides the centripetally collapsing transient crater floor (Figure 11). This results in a ring of structurally uplifted basement (peak ring) with an average diameter of ~0.5D (Pike, 1985). A consequence of central uplift rise is the downward sagging of the crater floor around the central peak or peak ring, forming an annular trough that is covered by impact breccias. The crater basement comprising the outer parts of the peak ring and the annular trough together define an asymmetric synform with a steep overturned inner limb and a shallow outer limb (Figures 7 and 11).

Extrapolation from scaling relationships obtained from craters on the Moon and other planets suggests that peak-ring craters should, in turn, transition to multi-ring impact basins on Earth at $D \sim 100$ km. While deep erosion and post-impact tectonics have destroyed any such evidence in the Vredefort and Sudbury impact structures, seismic imaging of the 180 km Chicxulub crater (Morgan et al., 2000) illustrates that the outer rings in such basins represent terraces produced by a series of concentric, inward-dipping, fault scarps of the crater rim region, but that the inner ring comprises centrifugally collapsed central uplift material.

Peak rings in craters on the Moon (e.g., Schrödinger) are expressed as rugged mountains that rise to several kilometers above the surrounding crater surface, exposing crater basement at elevations above the top of the impact melt sheet and crater fill breccias. Debate exists as to whether structural peak rings in terrestrial craters also have topographic expression, owing to Earth's greater gravity. Chicxulub contains a broad (~10 km wide) topographic peak ring that is raised by a few hundred meters above the crater floor (Morgan et al., 2000); albeit, the M0077A drill core through the peak ring shows that the parautochthonous basement rocks are covered by an attenuated impact melt and crater fill breccia sequence (Riller et al., 2018). In the 100 km wide Popigai crater, the crystalline basement rocks of the peak ring are overlain by a sequence of allogenic lithic and suevitic crater fill breccias (Masaitis et al., 1999). Owing to its limited erosion (100–300 m), Popigai preserves several key morphological elements, including an elevated crater rim and a well-defined structural peak ring at $R = 25$ km that has caused some upward deflection and attenuation of the overlying crater fill breccias (Masaitis et al., 1999, 2005). Geophysical modeling and drilling have established that the peak ring separates a 2.5 km deep inner basin from the 1.3–2 km deep annular trough (Masaitis et al., 1999, 2005); however, the crater floor in both the inner basin and annular trough shows local bathymetric changes of up to several hundred meters, reflecting faulting and the crater basement in the peak ring also shows internal fault block displacements of 100–200 m (Masaitis et al., 1999). In the annular trough, the crater fill breccias overlie centripetally slumped, fault-bounded blocks of crystalline basement and younger supracrustal units.

In the 85 km wide Manicouagan impact structure, glacial erosion of up to several hundred meters has degraded the original crater morphology and removed the fallback breccias and upper ~150 m of the melt sheet (Spray & Thompson, 2008). Most of the crater interior ($R \leq 22.5$ km) is covered by the melt sheet, which has an average remaining thickness of ~250 m (O'Connell-Cooper & Spray, 2011) but which is interrupted by a large (20 × 23 km), horseshoe-shaped block of uplifted crystalline basement at $R \sim 11.5$ km. Grieve and Head (1983) described Manicouagan as a peak-ring crater; however, Spray and Thompson (2008) have pointed out that the radial position of this horst block is inconsistent with that of a peak ring. Based on extensive drilling data, Spray and Thompson (2008) proposed that the inner crater floor is castellated, with a deep interior trough that is flanked by the uplifted block. They interpreted sharp changes in the crater floor bathymetry to steeply dipping faults with slip displacements ranging from hundreds of meters up to >1 km. It is not clear if these faults were exclusively generated during the impact or if they could represent reactivated pre-impact basement faults. Spray and Thompson (2008) proposed several alternative scenarios in which centripetal convergence and/or centrifugal divergence of fault-bounded blocks during the impact could produce the observed morphology and cautioned that despite the statistically derived morphometric relationships from the crater database and broad agreement between empirical observations of complex craters and hydrodynamic models of central uplift collapse, the internal structure of each crater needs to be carefully evaluated.

Effect of Erosion Level on Crater Size Estimates

Owing to their overall shallow basin morphology, even small amounts of erosion may significantly alter the morphometric parameters of terrestrial impact craters. For instance, erosion of a complex crater should lead to a decrease in the apparent crater diameter but an increase in the apparent diameter of the central peak (Kenkmann, 2021). In contrast, the apparent diameters of a peak ring and its adjacent annular trough axis could conceivably decrease markedly with erosion (e.g., Holm-Alwmark et al., 2017), although some craters appear to have true rim-to-rim diameters that are actually smaller than their apparent diameters (Collins, Kenkmann, et al., 2008; Holm-Alwmark et al., 2017).

If well-defined stratigraphic markers are not present in the target crust, estimating the depth of erosion of a degraded complex crater can be challenging, and will have significant implications for crater size estimates (e.g., Holm-Alwmark et al., 2017; Hough et al., 2003). Rae et al. (2017) and Holm-Alwmark et al. (2017) were able to use a combination of shock pressure attenuation profiles from both radial surface transects and multiple long drill cores at West Clearwater and Siljan to constrain erosion depths of, respectively, 2 and 4 km. The comparatively short M4 drill core intersection, which shows no obvious vertical attenuation effects, and the lack of surface exposures means that alternative sources are required to estimate the depth of erosion of the MIS.

The exhumation history of the interior plateau of southwestern Africa following the Morokweng impact is not rigorously constrained, but sedimentation patterns and sedimentation rates revealed by drilling of offshore fans along South Africa's West Coast, and differential erosion and thermochronology of kimberlite pipes intruded into the western Kaapvaal craton between 120 and 90 Ma, suggest regional Late Cretaceous to Cenozoic uplift and ensuing erosional exhumation of between 1 and 2 km (e.g., Hanson et al., 2009; Stanley et al., 2015, and references therein). Boulders of impact melt rock and shocked granite in the basal conglomerate of the Kalahari Group (e.g., Corner et al., 1997; Hart et al., 1997), and the absence of an upper chill margin in the impact melt sheet below the Kalahari Group unconformity (Andreoli et al., 1999; Hart et al., 1997; Reimold et al., 1999), indicate that the upper parts of the MIS crater fill sequence, which likely comprised several hundred meters of fallback suevites and breccias, as well as the upper parts of the melt sheet, have been eroded. The impact breccias reported in exploration boreholes at $R = 24$–29 km appear to be only sporadically preserved, which would be consistent with them being erosional remnants of crater fill deposits preserved in troughs overlying downfaulted basement blocks.

Based on Grieve and Pesonen's (1992) depth-to-diameter scaling formula, for a crater with a diameter in the 60–120 km range, the crater floor (top of the crater fill breccias) is likely to have lain ~1.0 km lower than the regional land surface immediately after impact. Kenny et al. (2021) proposed a pre-erosion melt sheet thickness of 1.13 km to reconcile the cooling history of the

Morokweng impact melt sheet derived from high-precision U–Pb zircon thermochronology. The 800 m of remaining melt sheet in the M3 drill core (Figure 1b) would thus require post-impact erosion of the uppermost ~300 m of the melt sheet. Together with the missing overlying crater fill breccias, this suggests that post-146 Ma erosion in the MIS must have exceeded ~1.5 km, which would be consistent with the upper range of estimates proposed by Hanson et al. (2009) and Stanley et al. (2015).

Evidence of an Eroded Peak Ring in the MIS

The most striking geophysical feature of the MIS is the slightly elliptical, $R = 15 \pm 2.5$ km, central positive magnetic anomaly (Ring I, Figure 1a), which Henkel et al. (2002) correlated with the present areal extent of the impact melt sheet beneath the Kalahari Group sediments. At $R = 18$ km, the M4 drill site lies immediately beyond this ring. The absence of impact melt in the M4 drill core (Gibson et al., 2024) contrasts with the thick melt sheet intersections in the four cores drilled at $R < 15$ km (Figure 1b) and provides independent corroboration of Henkel et al.'s (2002) interpretation. A comparison of the drill core logs further establishes that the basement rocks at the M4 site lie a minimum of 775 m higher than at the M3 site, despite only 4 km of radial difference between the two drill sites (Figure 1). Combined, these features support the M4 drill core corresponding to a concentric rampart of an uplifted crater basement surrounding a central basin filled by the impact melt sheet. The corresponding morphology—involving a deep, melt-filled, inner basin and surrounding peak ring—in both the Chicxulub (Morgan et al., 2000) and Popigai (Masaitis et al., 1999) craters, locates the peak ring at ~0.5D.

The petrographic and structural evidence that the M4 drill core rocks experienced moderately high levels of shock as well as ubiquitous evidence of post-shock, but impact-related, brittle deformation (fractures, shear faults, cataclasites, suevitic, and pseudotachylitic breccias; Gibson et al., 2024; Wela, 2017) is similar to evidence from the M0077A drill core through the Chicxulub peak ring (Feignon et al., 2020; Rae et al., 2019; Riller et al., 2018). Shock pressure estimates are higher than those obtained for the parautochthonous basement in the Popigai peak ring (8–10 GPa; Masaitis et al., 1999). Although no structural peak ring has been identified at Manicouagan, Murtaugh (1976) and Dressler (1990) established that "planar features" (including PDFs) indicative of peak shock pressures of up to 15 GPa are present in quartz, plagioclase and alkali feldspar up to $R = 20$–23 km (i.e., ~0.5D), which is both the outer limit of the partially eroded impact melt sheet and the predicted position that a peak ring would occupy in an 85 km diameter crater. Rae et al. (2017) and Holm-Alwmark et al. (2017) also estimate similar shock pressures of 15–18 GPa at ~0.5D in the West Clearwater and Siljan craters, respectively. In contrast, the uplifted faulted basement block at $R = 11.5$ km (i.e., 0.25D) in the Manicouagan crater is characterized by diaplectic quartz and feldspar glasses, indicating considerably higher peak shock pressures (>35 GPa; Dressler, 1970; Murtaugh, 1976) that are consistent with its more central location (compare Figures 7 and 8).

Shear faults in the M0077A drill core show dominantly normal dip-slip displacements, which Riller et al. (2018) attributed to its location near the outer toe of the Chicxulub peak ring. This contrasts with the predominantly reverse dip-slip displacements observed in the M4 drill core (Gibson et al., 2019, 2024); however, Riller et al. (2018) did report some reverse-slip faults toward the bottom of the M0077A core. This might provide further qualitative support for a significant depth of erosion in the M4 drill core and MIS.

In combination, the structural elevation, moderately high shock levels and highly faulted—yet still largely coherent—nature of the crater basement intersected in the M4 drill core fit the salient characteristics of a parautochthonous peak ring setting within a complex impact crater. As a first-order approximation, and applying a suitably wide error margin to account for the broad nature of terrestrial peak rings, this suggests an original (*true*) rim diameter for the Morokweng crater of ~70 ± 10 km. This concurs with the geophysical interpretations of Henkel et al. (2002) and Westgate et al. (2021), of an *apparent* crater diameter of between 65 and 80 km for the MIS. In the final section, we examine whether numerical modeling can further refine estimates of the original diameter of the Morokweng crater.

Morokweng Crater Diameter Constraints from Numerical Modeling

In this section, the iSALE-2D hydrocode is used to explore the implications of the shock and internal morphological features of the MIS revealed by the M4 drill core for the original diameter of the Morokweng crater. A similar approach has been adopted for the significantly eroded Siljan (Holm-Alwmark et al., 2017) and West Clearwater (Rae et al., 2017) craters, although both these studies involved multiple boreholes and surface sampling sites. The five numerical simulation results shown in Figure 7, corresponding to 45, 65, 80, 100, and 120 km final crater diameters, all produce structurally uplifted basements at intermediate distances (respectively, 12, 16, 20, 25, and 30 km) from the crater center, meeting the first requirement revealed by the M4 drill core data.

Impact melt volume is regarded as one of the most reliable impact cratering parameters derived from iSALE modeling (Manske et al., 2022; Pierazzo et al., 1997;

Wünnemann et al., 2008). The total melt volume produced and the volume of melt retained in the melt sheet are strongly controlled by a combination of impact parameters, such as the impactor size, velocity, and obliquity. In vertical impacts, melt volumes scale with impact energy, that is, linearly with projectile size and quadratically with velocity (Bjorkman & Holsapple, 1987; Pierazzo et al., 1997; Wünnemann et al., 2008). Given that crater dimensions scale with a combination of impact energy and momentum (O'Keefe & Ahrens, 1994), in craters of equivalent size, a small high-velocity projectile would thus produce more melt than a large low-velocity projectile. At a constant velocity and projectile size, less melt is produced, and a higher proportion of melt is ejected, as the impact angle decreases (Anderson et al., 2004; Pierazzo & Melosh, 2000). Table 4 and Figure 10 use a vertical impact and the most conservative impact velocity for the Morokweng impact to account for impactor survivability and impactor contribution in the melt sheet (McDonald et al., 2001; Potter & Collins, 2013). They show that melt volume increases exponentially with increasing crater size.

Table 4 shows that the volume of melt retained in the crater for the conservative impact scenario adopted for Morokweng varies from $<500\,\mathrm{km}^3$ in a 65 km diameter crater to $>1100\,\mathrm{km}^3$ in an 80 km diameter crater. O'Connell-Cooper and Spray (2011) estimated that a minimum melt sheet thickness of 500 m is required for internal differentiation to occur. All four boreholes through the MIS melt sheet show evidence of differentiation (Andreoli et al., 1999; Hart et al., 2002). Using this figure and assuming a cylindrical melt sheet with a diameter of 30 km implies a minimum Morokweng melt sheet volume of $350\,\mathrm{km}^3$. Potter and Collins (2013) used Hart et al.'s (2002) estimate of an 870 m thick melt sheet in their modeling. Although only 800 m of melt rock is actually intersected in the M3 drill core (Figure 1b shows that the uppermost 70 m of the core comprises Kalahari Group sediments), the upper parts of the melt sheet are clearly missing in all four centrally located drill holes (Hart et al., 1997, 2002), so the overestimate is not inconsistent with expectations and would result in a minimum retained melt volume of $\sim615\,\mathrm{km}^3$. Kenny et al. (2021) proposed an original MIS melt sheet thickness of 1.13 km to reconcile its modeled cooling history derived from high-precision U–Pb zircon thermochronology, which results in a volume of $\sim800\,\mathrm{km}^3$. Both these estimates lie between the predictions of the 65 and 80 km diameter crater simulations (Table 4; Figure 10), and assuming that the overwhelming bulk of the retained melt is found in the melt sheet, they support an original crater diameter in this range.

Although studies such as Masaitis et al. (1999) and Spray and Thompson (2008) demonstrate that the bathymetry of the melt sheet footwall is likely to be highly variable as a result of impact-related fault block displacements, the 60 GPa shock isobar in the simulations can be used to predict the approximate depth of the base of the melt sheet (Pierazzo et al., 1997). In the 65 km diameter scenario, no melt is predicted at $R = 18$ km, even before erosion (Figure 9a). While that is consistent with the lack of evidence of impact melt in the M4 drill core (Gibson et al., 2024), a pre-erosion melt sheet thickness of only ~600 m is predicted for the M3 drill core ($R = 14$ km; Figure 9b). As at least part of the melt sheet is eroded, and as regional estimates suggest at least 1.5 km of post-impact erosion, the evidence in the M3 drill core supports a larger diameter crater. In contrast, the 80 km diameter simulation predicts ~1 km of impact melt at $R = 18$ km, and 1.4 km at $R = 14$ km (Figure 9). Under this scenario, 2 km of post-impact erosion would be necessary to explain the lack of impact melt in the M4 drill core, but this would leave only ~400 m of impact melt at $R = 14$ km, which contradicts the evidence in the M3 drill core. At a first-order approximation, the simulation results thus suggest that the optimal original Morokweng crater diameter lies between 70 and 80 km; that is, somewhat larger than the 65–70 km apparent diameter estimated from the geophysical anomaly.

The absence or restricted occurrence of impact melt in both the Siljan and West Clearwater structures led Holm-Alwmark et al. (2017) and Rae et al. (2017) to estimate both erosion depths and crater diameter based on comparison of the observed shock pressure distribution pattern across the central parts of the respective impact structures with predicted shock pressures from iSALE simulations. The single reference point provided by the M4 drill core provides a less rigorous control; however, a basic comparison is nonetheless possible. Figure 8 shows that the bulk (>80%) of the modeled rock volume at $R = 18$ km in the 65 km diameter scenario would experience peak shock pressures below the 15–16 GPa estimate from the M4 drill core samples. Conversely, in the 80 km diameter scenario, the entire volume is predicted to experience peak pressures of >20 GPa, with ~50% experiencing pressures >30 GPa. While this supports the conclusions of an original crater diameter between 65 and 80 km derived from the melt sheet volume and distribution, it is important to note that several studies in other craters have noted that the shock pressure values predicted in iSALE are consistently 5–10 GPa higher than the values derived from shock barometry samples (Holm-Alwmark et al., 2017; Rae et al., 2017, 2019). This discrepancy must relate to either an inherent overestimation of the true shock pressures by iSALE, or an underestimation of the true shock pressures by shock barometry methods and their calibration; it might, at least in part, also reflect the disparity in scale between the empirical and modeled volumes (Rae et al., 2019). In the latter case, for reasons of computational efficiency, the data shown in Figures 8 and 9 derive from a block with dimensions of 2 × 2 km, which is almost an order of magnitude larger than the length of the basement succession intersected in the M4 drill core. It is also important to note that structural continuity is a fundamental assumption of iSALE models and, thus, it is unable to show fault-related disruption of the shock isobar pattern, despite this being inevitable during crater modification. Rae et al. (2017) have also pointed out that the volume of highly shocked crater basement showing diaplectic feldspar and quartz glasses is typically far smaller than model predictions, indicating that the smoothly attenuating shock profiles shown in Figure 9 are not matched in reality. This is borne out particularly well in the M0077A drill core where impact melt (≥60 GPa) lies directly over basement that shows peak shock pressures of only 16–18 GPa (Feignon et al., 2020). Finally, as discussed above, shock pressure may be underestimated if post-impact hydrothermal metamorphism causes selective annealing of high-angle PDFs (Grieve et al., 1990, 1996).

We conclude that the M4 drill core observations and data best fit a crater with an original rim-to-rim diameter of between 70 and 80 km in which a peak ring formed by dynamic outward collapse of the overheightened central uplift (Alexopoulos & McKinnon, 1994; Morgan et al., 2016; Murray, 1980), as borne out by numerical modeling. Particle trajectory analysis from the modeling (Figure 11) suggests that the M4 core rocks originated at a depth of 7–8 km and $R = 8$–9 km at the time of impact. Exhumation of rocks from this depth is more compatible with the final crater size than the 4 km vertical uplift proposed from geophysical modeling by Henkel et al. (2002). Further refinement of the crater diameter estimate would be assisted by: (a) petrographic and shock barometry analysis of more drill cores from the MIS; (b) one or more radial reflection seismic profiles across the MIS; (c) tighter constraints on the general depth of erosion of the MIS; (c) better understanding of the extent to which subsequent hydrothermal alteration could preferentially destroy high-angle PDFs and thus lead to underestimation of peak shock pressure; (d) better calibration of shock pressure estimates between numerical impact simulations and observational data; and (e) constraining the extent of structural disruption of shock isobars by impact-induced faults showing a consistent reverse-slip sense of displacement that affect the interval in the M4 core (Gibson et al., 2019).

CONCLUSIONS

Moderately shocked Archean granitoid gneisses intersected beneath Kalahari Group sediments in the M4 drillhole 18 km NNW of the estimated center of the Morokweng geophysical anomaly are interpreted as belonging to the structurally elevated, partially eroded, peak ring volume of a complex impact crater. Shock barometry from PDFs in quartz suggest that peak shock pressure reached ~16 GPa, consistent with a rock volume originally located close to the transient crater wall that was then displaced upwards and outwards during the crater modification stage. Numerical modeling supports Morokweng being a peak-ring crater with a final rim diameter of 70–80 km, slightly larger than the apparent rim diameter of 65–70 km. Shock pressures recorded in the M4 drill core are significantly higher than those recorded in parautochthonous basement in the Popigai peak ring, but slightly lower than those obtained from the M0077A drill core through the Chicxulub peak ring. Notwithstanding the apparently smaller size of the MIS relative to Chicxulub, this may reflect the deeper erosion and/or more intense impact-induced hydrothermal alteration that may have preferentially destroyed high-index PDFs in the M4 core.

Acknowledgments—This work is based on research supported in part by the National Research Foundation of South Africa Grant SRUG200503519568 to RG. MA acknowledges prior financial support from the NRF Rated Researcher Program and SW was supported by a University of the Witwatersrand Postgraduate Merit Award. ASPR acknowledges funding from Trinity College, University of Cambridge. Research access to the M4 core by Mr. S. Dhlomo, Senior Manager, NLM-Necsa, is gratefully acknowledged. C. Majola prepared the thin sections and T. Masiu and L. Malelu assisted with photography. S. Alwmark and M. Poelchau are thanked for their constructive reviews.

Data Availability Statement—Data available on request from the authors.

Editorial Handling—Dr. Michael H. Poelchau

REFERENCES

Agarwal, A., Poelchau, M. H., Kenkmann, T., Rae, A., and Ebert, M. 2019. Impact Experiment on Gneiss: The Effects of Foliation on Cratering Process. *Journal of Geophysical Research: Solid Earth* 124: 13532–46. https://doi.org/10.1029/2019JB018345.

Alexopoulos, J. S., and McKinnon, W. B. 1994. Large Impact Craters and Basins on Venus, with Implications for Ring Mechanics on the Terrestrial Planets. In *Large Meteorite Impacts and Planetary Evolution*, edited by B. O. Dressler, R. A. F. Grieve, and V. L. Sharpton. GSA Special Paper 293, 29–50. Boulder, CO: Geological Society of America.

Amsden, A. A., Ruppel, H. M., and Hirt, C. W. 1980. *SALE: A Simplified ALE Computer Program for Fluid Flow at all*

Speeds (LA-8095). New Mexico: Los Alamos National Laboratories.
Anderson, J. L., Schultz, P. H., and Heineck, J. T. 2004. Experimental Ejection Angles for Oblique Impacts: Implications for the Subsurface Flow-Field. *Meteoritics & Planetary Science* 39: 303–320.
Andreoli, M. A. G., Ashwal, L. D., Hart, R. J., and Huizenga, J. M. 1999. A Ni and PGE-Enriched Quartz Norite Impact Melt Complex in the Late Jurassic Morokweng Impact Structure, South Africa. In *Large Meteorite Impacts and Planetary Evolution II*, edited by B. O. Dressler, and V. L. Sharpton. GSA Special Paper 339, 91–108. Boulder, CO: Geological Society of America.
Andreoli, M. A. G., Ashwal, L. D., Hart, R. J., Smith, C. B., Webb, S. J., Tredoux, M., Gabrielli, F., Cox, R., and Hambleton-Jones, B. B. 1995. The Impact Origin of the Morokweng Ring Structure, Southern Kalahari, South Africa. *Geological Society of South Africa Centennial Geocongress, Johannesburg, Extended Abstract* I: 541–44.
Andreoli, M. A. G., Hart, R. J., Cooper, G., and Webb, S. 2008. The Morokweng Impact Crater, South Africa: A Large Complex, Multiring Structure with a ~130 Km Radius External Ring and Asymmetric Radial Sectors. *Large Meteorite Impacts and Planetary Evolution IV*, abstract 3048.
Andreoli, M. A. G., Hart, R. J., Cooper, G. R. J., Stengel, I., Webb, S., Haddon, I., Skala, R., and Viola, G. 2007. The 144 Ma Morokweng Impact Crater, South Africa: Geophysical and Borehole Evidence for a ~240 km Structure. In *10th SAGA Biennial Conference*, p. 4.
Artemieva, N. A., Wünnemann, K., Krien, F., Reimold, W. U., and Stöffler, D. 2013. Ries Crater and Suevite Revisited—Observations and Modeling Part II: Modeling. *Meteoritics & Planetary Science* 48: 590–627. https://doi.org/10.1111/maps.12085.
Benz, W., Cameron, A., and Melosh, H. 1989. The Origin of the Moon and the Single-Impact Hypothesis III. *Icarus* 81: 113–131.
Bjorkman, M. D., and Holsapple, K. A. 1987. Velocity Scaling Impact Melt Volume. *International Journal of Impact Engineering* 5: 155–163.
Collins, G. S. 2014. Numerical Simulations of Impact Crater Formation with Dilatancy. *Journal of Geophysical Research: Planets* 119: 2600–2619. https://doi.org/10.1002/2014JE004708.
Collins, G. S., Kenkmann, T., Osinski, G. R., and Wünnemann, K. 2008. Mid-Sized Complex Crater Formation in Mixed Crystalline-Sedimentary Targets: Insight from Modelling and Observation. *Meteoritics & Planetary Science* 43: 1955–77.
Collins, G. S., Morgan, J., Barton, P., Christeson, G. L., Gulick, S., Urrutia, J., Warner, M., and Wünnemann, K. 2008. Dynamic Modeling Suggests Terrace Zone Asymmetry in the Chicxulub Crater Is Caused by Target Heterogeneity. *Earth and Planetary Science Letters* 270: 221–230. https://doi.org/10.1016/j.epsl.2008.03.032.
Collins, G. S., and Wünnemann, K. 2005. How Big Was the Chesapeake Bay Impact? Insight from Numerical Modeling. *Geology* 33: 925–28. https://doi.org/10.1130/G21854.1.
Corner, B., Reimold, W. U., Brandt, D., and Koeberl, C. 1997. Morokweng Impact Structure, Northwest Province, South Africa: Geophysical Imaging and some Preliminary Shock Petrographic Studies. *Earth and Planetary Science Letters* 146: 351–364.
Cox, M. A., Erickson, T. M., Schmieder, M., Christoffersen, R., Ross, D. K., Cavosie, A. J., Bland, P. A., Kring, D. A., and IODP–ICDP Expedition 364 Scientists. 2020. High Resolution Microstructural and Compositional Analyses of Shock Deformed Apatite from the Peak Ring of the Chicxulub Impact Crater. *Meteoritics & Planetary Science* 55: 1715–33. https://doi.org/10.1111/maps.13541.
Davison, T. M., and Collins, G. S. 2022. Complex Crater Formation by Oblique Impacts on the Earth and Moon. *Geophysical Research Letters* 49: e2022GL101117. https://doi.org/10.1029/2022GL101117.
Dressler, B. 1970. Shock Metamorphic Features and Their Zoning and Orientation in the Precambrian Rocks of the Manicouagan Structure, Quebec, Canada. *Tectonophysics* 171: 229–245.
Dressler, B. 1990. Shock Metamorphic Features and their Zoning and Orientation in the Precambrian Rocks of the Manicouagan Structure, Quebec, Canada. *Tectonophysics* 171: 229–245. https://doi.org/10.1016/0040-1951(90)90101-D.
Dressler, B. O., Sharpton, V. L., and Schuraytz, B. C. 1998. Shock Metamorphism and Shock Barometry at a Complex Impact Structure: Slate Islands, Canada. *Contributions to Mineralogy and Petrology* 130: 275–287.
Ebert, M., Poelchau, M. H., Kenkmann, T., Gulick, S. P. S., Hall, B., Lofi, J., McCall, N., and Rae, A. S. P. 2021. Comparison of Stress Orientation Indicators in Chicxulub's Peak Ring: Kinked Biotites, Basal PDFs, and Feather Features. In *Large Meteorite Impacts and Planetary Evolution VI*, edited by W. U. Reimold, and C. Koeberl. GSA Special Paper 550, 479–493. Boulder, CO: Geological Society of America. https://doi.org/10.1130/2021.2550(21).
Ebert, M., Poelchau, M. H., Kenkmann, T., and Schuster, B. 2020. Tracing Shock Wave Propagation in the Chicxulub Crater: Implications for the Formation of Peak Rings. *Geology* 48: 814–18. https://doi.org/10.1130/G47129.1.
Engelhardt, W. V., and Bertsch, W. 1969. Shock Induced Planar Deformation Structures in Quartz from the Ries Crater, Germany. *Contributions to Mineralogy and Petrology* 20: 203–234.
Engelhardt, W. V., Hörz, F., Stöffler, D., and Bertsch, W. 1968. Observations on Quartz Deformation in the Breccias of West Clearwater Lake, Canada and the Ries Basin, Germany. In *Shock Metamorphism of Natural Materials*, edited by B. M. French, and N. M. Short, 475–482. Baltimore, MD: Maryland, Mono Book Corporation.
Feignon, J.-G., Ferrière, L., Leroux, H., and Koeberl, C. 2020. Characterization of Shocked Quartz Grains from Chicxulub Peak Ring Granites and Shock Pressure Estimates. *Meteoritics & Planetary Science* 55: 2206–23.
Feldman, V. I. 1994. The Conditions of Shock Metamorphism. In *Large Meteorite Impacts and Planetary Evolution*, edited by B. O. Dressler, R. A. F. Grieve, and V. L. Sharpton. GSA Special Paper 293, 121–132. Boulder, CO: Geological Society of America.
Feldman, V. I., Sazonova, L. V., and Kotel'nikov, S. I. 1996. Distribution of the Shock Pressure in the Rocks of the Vorotilov Hole, Puchezh-Katunki Astrobleme. *Doklady Akademii Nauk SSSR* 349: 658–660.
Ferrière, L., Koeberl, C., Ivanov, B. A., and Reimold, W. U. 2008. Shock Metamorphism of Bosumtwi Impact Crater

Rocks, Shock Attenuation, and Uplift Formation. *Science* 322: 1678–81.

Ferrière, L., Morrow, J. R., Amgaa, T., and Koeberl, C. 2009. Systematic Study of Universal-Stage Measurements of Planar Deformation Features in Shocked Quartz: Implications for Statistical Significance and Representation of Results. *Meteoritics & Planetary Science* 44: 925–940.

French, B. M. 1998. *Traces of Catastrophe: A Handbook of Shock-Metamorphic Effects in Terrestrial Meteorite Impact Structures*. Lunar and Planetary Institute Contribution No. 954. Houston, TX: Lunar and Planetary Institute, p. 120.

French, B. M., and Koeberl, C. 2010. The Convincing Identification of Terrestrial Meteorite Impact Structures: What Works, What doesn't, and why. *Earth-Science Reviews* 98: 123–170.

French, B. M., Koeberl, C., Gilmour, I., Shirey, S. B., Dons, J. A., and Naterstad, J. 1997. The Gardnos Impact Structure, Norway: Petrology and Geochemistry of Target Rocks and Impactites. *Geochimica et Cosmochimica Acta* 61: 873–904. https://doi.org/10.1016/S0016-9697037(96)00382-1.

Gibson, R. L., and Reimold, W. U. 2005. Shock Pressure Distribution in the Vredefort Impact Structure, South Africa. In *Large Meteorite Impacts III*, edited by T. Kenkmann, F. Hörz, and A. Deutsch. GSA Special Paper 384, 329–349. Boulder, CO: Geological Society of America.

Gibson, R. L., Wela, S. S., and Andreoli, M. A. G. 2019. Structural Analysis of the M4 Drill Core, Morokweng Impact Structure (South Africa)—Implications for Peak Ring Formation Processes. *Large Meteorite Impacts and Planetary Evolution VI*, abstract #5051.

Gibson, R. L., Wela, S. S., Bybee, G. M., Frei, D., and Andreoli, M. A. G. 2022. Granitoid Gneisses of the Morokweng Impact Structure: Implications for Neoarchaean Evolution of the Western Kaapvaal Craton. *Lithos* 426-427: 106793. https://doi.org/10.1016/j.lithos.2022.106793.

Goldin, T. J., Wünnemann, K., Melosh, H. J., and Collins, G. S. 2006. Hydrocode Modelling of the Sierra Madera Impact Structure. *Meteoritics & Planetary Science* 41: 1947–58.

Goltrant, O., Leroux, H., Doukhan, J.-C., and Cordier, P. 1992. Formation Mechanisms of Planar Deformation Features in Naturally Shocked Quartz. *Physics of the Earth and Planetary Interiors* 74: 219–240.

Gibson, R. L., Wela, S. S., Vonopartis, L. C., and Andreoli, M. A. G. 2024. Melt Breccias in Parautochthonous Basement Rocks of the Morokweng Impact Structure, South Africa – Evidence for a Friction Origin. *Journal of African Earth Sciences* 214: 105239.

Grieve, R. A. F. 1991. Terrestrial Impact: The Record in the Rocks. *Meteoritics* 26: 175–194.

Grieve, R. A. F., and Cintala, M. 1997. Planetary Differences in Impact Melting. *Advances in Space Research* 20: 1551–60.

Grieve, R. A., Langenhorst, F., and Stöffler, D. 1996. Shock Metamorphism of Quartz in Nature and Experiment: II. Significance in Geoscience. *Meteoritics & Planetary Science* 31: 6–35.

Grieve, R. A., Reimold, W. U., Morgan, J., Riller, U., and Pilkington, M. 2008. Observations and Interpretations at Vredefort, Sudbury, and Chicxulub: Towards an Empirical Model of Terrestrial Impact Basin Formation. *Meteoritics & Planetary Science* 43: 855–882.

Grieve, R. A. F., Coderre, J. M., Robertson, P. B., and Alexopoulos, J. 1990. Microscopic Planar Deformation Features in Quartz of the Vredefort Structure: Anomalous but Still Suggestive of an Impact Origin. *Tectonophysics* 171: 185–200.

Grieve, R. A. F., and Head, J. W. 1983. The Manicouagan Impact Structure: An Analysis of its Original Dimensions and Form. *Journal of Geophysical Research* 88: 807–818.

Grieve, R. A. F., and Pesonen, L. J. 1992. The Terrestrial Impact Record. *Tectonophysics* 216: 1–30.

Grieve, R. A. F., and Robertson, P. B. 1976. Variations in Shock Deformation at the Slate Islands Impact Structure, Lake Superior, Canada. *Contributions to Mineralogy and Petrology* 58: 37–49.

Hanson, E. K., Moore, J. M., Bordy, E. M., Marsh, J. S., Howarth, G., and Robey, J. V. A. 2009. Cretaceous Erosion in Central South Africa: Evidence from Upper-Crustal Xenoliths in Kimberlite Diatremes. *South African Journal of Geology* 112: 125–140.

Harris, R. S., Jaret, S. J., Rodesney, S. N., King, D. T., and Schultz, P. H. 2010. Alternate Twin Deformation of Plagioclase at Low Shock Pressures: Implications for Recognizing and Interpreting Impacts in Basalt. *AGU Meeting of the Americas*, abstract P41A-03.

Hart, R. J., Andreoli, M. A. G., Tredoux, M., Moser, D., Ashwal, L. D., Eide, E., Webb, S. J., and Brandt, D. 1997. Late Jurassic Age for the Morokweng Impact Structure, Southern Africa. *Earth and Planetary Science Letters* 147: 25–35.

Hart, R. J., Cloete, M., McDonald, I., Carlson, R. W., and Andreoli, M. A. G. 2002. Siderophile-Rich Inclusions from the Morokweng Impact Melt Sheet, South Africa: Possible Fragments of a Chondritic Meteorite. *Earth and Planetary Science Letters* 198: 49–62.

Henkel, H., Reimold, W. U., and Koeberl, C. 2002. Magnetic and Gravity Model of the Morokweng Impact Structure. *Journal of Applied Geophysics* 49: 129–147.

Holm-Alwmark, S., Ferrière, L., Alwmark, C., and Poelchau, M. H. 2018. Estimating Average Shock Pressures Recorded by Impactite Samples Based on Universal Stage Investigations of Planar Deformation Features in Quartz—Sources of Error and Recommendations. *Meteoritics & Planetary Science* 53: 110–130.

Holm-Alwmark, S., Rae, A. S. P., Ferrière, L., Alwmark, C., and Poelchau, M. H. 2017. Combining Shock Barometry with Numerical Modeling: Insights into Complex Crater Formation—The Example of the Siljan Impact Structure (Sweden). *Meteoritics & Planetary Science* 52: 2521–49. https://doi.org/10.1111/maps.12955.

Holsapple, K. 1993. The Scaling of Impact Processes in Planetary Sciences. *Annual Review of Earth and Planetary Sciences* 21: 333–373.

Hörz, F. 1968. Statistical Measurements of Deformation Structures and Refractive Indices in Experimentally Shock Loaded Quartz. In *Shock Metamorphism of Natural Materials*, edited by B. M. French, and N. M. Short, 243–253. Baltimore, MD: Mono Book Corporation.

Hough, R. M., Lee, M. R., and Bevan, A. W. R. 2003. Characterization and Significance of Shocked Quartz from the Woodleigh Impact Structure, Western Australia. *Meteoritics & Planetary Science* 38: 1341–50.

Huber, M. S., Ferrière, L., Losiak, A., and Koeberl, C. 2011. ANIE: A Mathematical Algorithm for Automated Indexing of Planar Deformation Features in Quartz Grains. *Meteoritics & Planetary Science* 46: 1418–24.

Ivanov, B. A. 2005. Numerical Modeling of the Largest Terrestrial Meteorite Craters. *Solar System Research* 39: 381–409.

Ivanov, B. A., Deniem, D., and Neukum, G. 1997. Implementation of Dynamic Strength Models into 2D Hydrocodes: Applications for Atmospheric Breakup and Impact Cratering. *International Journal of Impact Engineering* 17: 375–386. https://doi.org/10.1016/S0734-743X(97)87511-2.

Jaret, S. J., Hemming, S. R., Rasbury, E. T., Thompson, L. M., Glotch, T. D., Ramezani, J., and Spray, J. G. 2018. Context Matters—Ar-Ar Results from in and around the Manicouagan Impact Structure, Canada: Implications for Martian Meteorite Chronology. *Earth and Planetary Science Letters* 501: 78–89.

Jaret, S. J., Kah, L. C., and Harris, R. S. 2014. Progressive Deformation of Feldspar Recording Low Barometry Impact Processes, Tenoumer Impact Structure, Mauritania. *Meteoritics & Planetary Science* 49: 1007–22. https://doi.org/10.1111/maps.12310.

Kenkmann, T. 2021. The Terrestrial Impact Crater Record: A Statistical Analysis of Morphologies, Structures, Ages, Lithologies, and More. *Meteoritics & Planetary Science* 56: 1024–70.

Kenkmann, T., Collins, G. S., Wittmann, A., Wünnemann, K., Reimold, W. U., and Melosh, H. J. 2009. A Model for the Formation of the Chesapeake Bay Impact Crater as Revealed by Drilling and Numerical Simulation. In *The ICDP-USGS Deep Drilling Project in the Chesapeake Bay Impact Structure: Results from the Eyreville Core Holes*, edited by G. S. Gohn, C. Koeberl, K. G. Miller, and W. U. Reimold. GSA Special Paper 458, 571–585. Boulder, CO: Geological Society of America. https://doi.org/10.1130/2009.2458(25).

Kenny, G. G., Harrigan, C. O., Schmitz, M. D., Crowley, J. L., Wall, C. J., Andreoli, M. A. G., Gibson, R. L., and Maier, W. D. 2021. Timescales of Impact Melt Sheet Crystallization and the Precise Age of the Morokweng Impact Event, South Africa. *Earth and Planetary Science Letters* 567: 117013. https://doi.org/10.1016/j.epsl.2021.117013.

Koeberl, C., Armstrong, R. A., and Reimold, W. U. 1997. Morokweng, South Africa: A Large Impact Structure of Jurassic-Cretaceous Boundary Age. *Geology* 25: 731–34.

Koeberl, C., and Reimold, W. U. 2003. Geochemistry and Petrography of Impact Breccias and Target Rocks from the 145 ma Morokweng Impact Structure, South Africa. *Geochemica et Cosmochimica Acta* 67: 1837–62.

LeFeuvre, M., and Wieczorek, M. A. 2011. Nonuniform Cratering of the Moon and a Revised Crater Chronology of the Inner Solar System. *Icarus* 214: 1–20.

Leroux, H., Reimold, W. U., and Doukhan, J.-C. 1994. A T.E.M. Investigation of Shock Metamorphism in Quartz from the Vredefort Dome, South Africa. *Tectonophysics* 230: 223–239.

Maier, W. D., Andreoli, M. A. G., McDonald, I., Higgins, M. D., Boyce, A. J., Shukolyukov, A., Lugmair, G. W., et al. 2006. Discovery of a 25 cm Asteroid Clast in the Giant Morokweng Impact Crater, South Africa. *Nature* 441: 203–6.

Manske, L., Wünnemann, K., and Kurosawa, K. 2022. Quantification of Impact-Induced Melt Production in Numerical Modeling Revisited. *Journal of Geophysical Research: Planets* 127: e2022JE007426.

Masaitis, V. L., Naumov, M. V., and Mashchak, M. S. 1999. Anatomy of the Popigai Impact Crater, Russia. In *Large Meteorite Impacts and Planetary Evolution II*, edited by B. O. Dressler, and V. L. Sharpton. GSA Special Paper 339, 1–18. Boulder, CO: Geological Society of America.

Masaitis, V. L., Naumov, M. V., and Mashchak, M. S. 2005. Original Diameter and Depth of Erosion of Popigai Impact Crater, Russia. In *Large Meteorite Impacts III*, edited by T. Kenkmann, F. Hörz, and A. Deutsch. GSA Special Paper 384, 131–140. Boulder, CO: Geological Society of America.

McDonald, I., Andreoli, M. A. G., Hart, R. J., and Tredoux, M. 2001. Platinum-Group Elements in the Morokweng Impact Structure South Africa: Evidence for the Impact of a Large Ordinary Chondrite Projectile at the Jurassic-Cretaceous Boundary. *Geochimica et Cosmochimica Acta* 65: 299–309.

Melosh, H. J. 1989. *Impact Cratering: A Geologic Process*. New York: Oxford University Press, p. 245.

Melosh, H. J., and Ivanov, B. A. 1999. Impact Crater Collapse. *Annual Reviews of Earth and Planetary Science* 27: 385–415.

Melosh, H. J., Ryan, E. V., and Asphaug, E. 1992. Dynamic Fragmentation in Impacts: Hydrocode Simulation of Laboratory Impacts. *Journal of Geophysical Research* 97 (E9): 14735–59. https://doi.org/10.1029/92JE01632.

Moreau, J., Kohout, T., and Wünnemann, K. 2017. Shock-Darkening in Ordinary Chondrites: Determination of the Pressure-Temperature Conditions by Shock Physics Mesoscale Modeling. *Meteoritics & Planetary Science* 52: 2375–90. https://doi.org/10.1111/maps.12935.

Morgan, J. V., Gulick, S. P. S., Bralower, T., Chenot, E., Christeson, G., Claeys, P., Cockell, C., et al. 2016. The Formation of Peak Rings in Large Impact Craters. *Science* 354: 878–882.

Morgan, J. V., Warner, M. R., Collins, G. S., Melosh, H. J., and Christeson, G. L. 2000. Peak-Ring Formation in Large Impact Craters: Geophysical Constraints from Chicxulub. *Earth and Planetary Science Letters* 183: 347–354.

Murray, J. B. 1980. Oscillating Peak Model of Basin and Crater Formation. *The Moon and the Planets* 22: 269–291. https://doi.org/10.1007/BF01259285.

Murtaugh, J. C. 1976. Manicouagan Impact Structure. *Quebec Department of Natural Resources, Open-File Report* DPV-432: 180.

O'Connell-Cooper, C. D., and Spray, J. G. 2011. Geochemistry of the Impact-Generated Melt Sheet at Manicouagan: Evidence for Fractional Crystallization. *Journal of Geophysical Research* 116: 1–22.

O'Keefe, J. D., and Ahrens, T. J. 1994. Impact-Induced Melting of Planetary Surfaces. In *Large Meteorite Impacts and Planetary Evolution*, edited by B. O. Dressler, R. A. F. Grieve, and V. L. Sharpton, *GSA Special Paper* 293, 103–9. Boulder, CO: Geological Society of America.

Ogilvie, P., Gibson, R. L., Reimold, W. U., Deutsch, A., and Hornemann, U. 2011. Experimental Investigation of Shock Metamorphic Effects in a Metapelitic Granulite: The Importance of Shock Impedance Contrast between Components. *Meteoritics & Planetary Science* 46: 1565–86.

Pati, J. K., Jourdan, F., Armstrong, R. A., Reimold, W. U., and Prakash, K. 2010. First SHRIMP U-Pb and $^{40}Ar/^{39}Ar$ Chronological Results from Melt Breccia from the Paleoproterozoic Dhala Impact Structure, India. In *Large Meteorite Impacts and Planetary Evolution IV*, edited by R. L. Gibson, and W. U. Reimold. GSA Special Paper 465, 571–591. Boulder, CO: Geological Society of America.
Pickersgill, A. E., Jaret, S. J., Pittarello, L., Fritz, J., and Harris, R. S. 2021. Shock Effects in Feldspars: An Overview. In *Large Meteorite Impacts and Planetary Evolution VI*, edited by W. U. Reimold, and C. Koeberl. GSA Special Paper 550, 507–535. Boulder, CO: Geological Society of America. https://doi.org/10.1130/2021.2550(23).
Pickersgill, A. E., Osinski, G. R., and Flemming, R. L. 2013. Shock Metamorphism in Plagioclase from the Mistastin Lake Impact Structure, Canada. *Proceedings, 44th Lunar and Planetary Science Conference*, p. 2471.
Pickersgill, A. E., Osinski, G. R., and Flemming, R. L. 2015. Shock Effects in Plagioclase Feldspar from the Mistastin Lake Impact Structure, Canada. *Meteoritics & Planetary Science* 50: 1546–61.
Pierazzo, E., and Melosh, H. J. 2000. Melt Production in Oblique Impacts. *Icarus* 145: 252–261.
Pierazzo, E., Vickery, A. M., and Melosh, H. J. 1997. A Reevaluation of Impact Melt Production. *Icarus* 127: 408–423. https://doi.org/10.1006/icar.1997.5713.
Poelchau, M. H., and Kenkmann, T. 2011. Feather Features: A Low-Shock-Pressure Indicator in Quartz. *Journal of Geophysical Research: Solid Earth* 116(B2): e2010JB007803. https://doi.org/10.1029/2010JB007803.
Pike, R. J. 1985. Some Morphologic Systematics of Complex Impact Structures. *Meteoritics* 20: 49–68.
Potter, R. W. K., and Collins, G. S. 2013. Numerical Modeling of Asteroid Survivability and Possible Scenarios for the Morokweng Crater-Forming Impact. *Meteoritics & Planetary Science* 48: 744–757. https://doi.org/10.1111/maps.12098.
Rae, A. S. P., Collins, G. S., Grieve, R. A. F., Osinski, G. R., and Morgan, J. V. 2017. Complex Crater Formation: Insights from Combining Observations of Shock Pressure Distribution with Numerical Models at the West Clearwater Lake Impact Structure. *Meteoritics & Planetary Science* 52: 1330–50. https://doi.org/10.1111/maps.12825.
Rae, A. S. P., Poelchau, M. H., and Kenkmann, T. 2021. Stress and Strain During Shock Metamorphism. *Icarus* 370: 114687.
Rae, A. S. P., Collins, G. S., Poelchau, M., and IODP-ICDP Expedition 364 Scientists. 2019. Stress-Strain Evolution during Peak-Ring Formation: A Case Study of the Chicxulub Impact Structure. *Journal of Geophysical Research: Planets* 124: 396–417. https://doi.org/10.1029/2018JE005821.
Reimold, W. U., Armstrong, R. A., and Koeberl, C. 2002. A Deep Drillcore from the Morokweng Impact Structure, South Africa: Petrography, Geochemistry and Constrains on the Crater Size. *Earth and Planetary Science Letters* 201: 221–232.
Reimold, W. U., Koeberl, C., Brandstatter, F., Armstrong, R. A., and Bootsman, C. 1999. The Morokweng Impact Structure, South Africa: Geologic, Petrographic and Isotopic Results, and Implications for the Size of the Structure. In *Large Meteorite Impacts and Planetary Evolution II*, edited by B. O. Dressler, and V. L. Sharpton. Geological Society of America Special Paper 339, 61–90. Boulder, CO: Geological Society of America.
Riller, U., Poelchau, M. H., Rae, A. S. P., Schulte, F. M., Collins, G. S., Melosh, H. J., and Expedition 364 Science Party, IODP-ICDP. 2018. Rock Fluidization during Peak-Ring Crater Formation. *Nature* 562: 511–18. https://doi.org/10.1038/s41586-018-0607-z.
Robertson, P. B., and Grieve, R. A. F. 1977. Shock Attenuation at Terrestrial Impact Structures. In *Impact and Explosion Cratering*, edited by D. J. Roddy, R. O. Pepin, and R. B. Merrill, 687–702. New York: Pergamon Press.
Rubin, A. E. 1992. A Shock-Metamorphic Model for Silicate Darkening and Compositionally Variable Plagioclase in CK and Ordinary Chondrites. *Geochimica et Cosmochimica Acta* 56: 1705–14. https://doi.org/10.1016/0016-7037(92)90236-C.
Singleton, A. C., Osinski, G. R., McCausland, P. J., and Moser, D. E. 2011. Shock-Induced Changes in Density and Porosity in Shock-Metamorphosed Crystalline Rocks, Haughton Impact Structure, Canada. *Meteoritics & Planetary Science* 46: 1774–86.
Smit, P. J. 1977. *Die Geohidrologie in die Opvanggebied van die Moloporivier in die Noordelijke Kalahari, Bloemfontein*. Unpublished Ph.D. Thesis, University of the Orange Free State, p. 354.
Spray, J. G., and Thompson, L. M. 2008. Constraints on Central Uplift Structure from the Manicouagan Impact Crater. *Meteoritics & Planetary Science* 43: 2049–57.
Stanley, J. R., Flowers, R. M., and Bell, D. R. 2015. Erosion Patterns and Mantle Sources of Topographic Change across the Southern African Plateau Derived from the Shallow and Deep Records of Kimberlites. *Geochemistry, Geophysics, Geosystems* 16: 3235–56.
Stöffler, D. 1967. Deformation und Umwandlung von Plagioklas durch Stoßwellen in den 1340 Gesteinen des Nördlinger Ries. *Contributions to Mineralogy and Petrology* 16: 51–83. https://doi.org/10.1007/BF00371608.
Stöffler, D. 1972. Deformation and Transformation of Rock Forming Minerals by Natural and Experimental Shock Processes: I. Behavior of Minerals under Shock Compression. *Fortschritte der Mineralogie* 49: 50–113.
Stöffler, D., Keil, K., and Scott, E. R. D. 1991. Shock Metamorphism of Ordinary Chondrites. *Geochimica et Cosmochimica Acta* 55: 3845–67.
Stöffler, D., and Langenhorst, F. 1994. Shock Metamorphism of Quartz in Nature and Experiment: I. Basic Observation and Theory. *Meteoritics* 29: 155–181.
Timms, N. E., Pearce, M. A., Erickson, T. M., Cavosie, A. J., Rae, A. S., Wheeler, J., Wittmann, A., et al. 2019. New Shock Microstructures in Titanite ($CaTiSiO_5$) from the Peak Ring of the Chicxulub Impact Structure, Mexico. *Contributions to Mineralogy and Petrology* 174: 38. https://doi.org/10.1007/s00410-019-1565-7.
Thompson, L. M., and Spray, J. G. 2017. Dynamic Interaction Between Impact Melt and Fragmented Basement at Manicouagan: The Suevite Connection. *Meteoritics & Planetary Science* 52: 1300–1329.
Turtle, E. P., Pierazzo, E., Collins, G. S., Osinski, G. R., Melosh, H. J., Morgan, J. V., and Reimold, W. U. 2005. Impact Structures: What Does Crater Diameter Mean? In *Large Meteorite Impacts III*, edited by T. Kenkmann, F.

Hörz, and A. Deutsch. GSA Special Paper 384, 1–24. Boulder, CO: Geological Society of America.
Vasconcelos, M., Wünnemann, K., Crósta, A., Molina, E., Reimold, W. U., and Yokoyama, E. 2012. Insights into Themorphology of the Serra da Cangalha Impact Structure from Geophysical Modeling. *Meteoritics & Planetary Science* 47: 1659–70.
Vasconcelos, M. A. R., Rocha, F. F., Crósta, A. P., Wünnemann, K., Güldemeister, N., Leite, E. P., Ferreira, J. C., and Reimold, W. U. 2019. Insights about the Formation of a Complex Impact Structure Formed in Basalt from Numerical Modeling: The Vista Alegre Structure, Southern Brazil. *Meteoritics & Planetary Science* 54: 2373–83. https://doi.org/10.1111/maps.13298.
Wela, S. S. 2017. *A Lithological, Petrographic and Geochemical Investigation of the M4 Borehole Core, Morokweng Impact Structure, South Africa*. MSc dissertation (unpublished), University of the Witwatersrand, p. 385.
Westgate, M., Manzi, M. S. D., Malehmir, A., Gibson, R. L., Andreoli, M. A. G., and Bumby, A. 2021. A Reappraisal of Legacy Reflection Seismic Data from the Western Margin of the Kaapvaal Craton, South Africa, with Implications for Mesozoic-Cenozoic Regional Tectonics. *Tectonophysics* 813: 2289134. https://doi.org/10.1016/j.tecto.2021.228934.
Whitehead, J., Spray, J. G., and Grieve, R. A. 2002. Origin of "Toasted" Quartz in Terrestrial Impact Structures. *Geology* 30: 431–34.
Williams, G. E., and Schmidt, P. W. 2021. Dating the Acraman Asteroid Impact, South Australia: The Case for Deep Drilling the 'Hot Shock' Zone of the Central Uplift. *Australian Journal of Earth Sciences* 68: 355–367. https://doi.org/10.1080/08120099.2020.1808066.
Wood, C. A., and Head, J. W. 1976. Multi-Ring Basins on Mars, Mercury and the Moon (abstract). Lunar Science VII, The Lunar Institute, Houston. pp. 930–932.
Wünnemann, K., Collins, G. S., and Melosh, H. J. 2006. A Strain-Based Porosity Model for Use in Hydrocode Simulations of Impacts and Implications for Transient Crater Growth in Porous Targets. *Icarus* 180: 514–527. https://doi.org/10.1016/j.icarus.2005.10.013.
Wünnemann, K., Collins, G. S., and Osinski, G. R. 2008. Numerical Modelling of Impact Melt Production in Porous Rocks. *Earth and Planetary Science Letters* 269: 530–39.
Wünnemann, K., and Ivanov, B. A. 2003. Numerical Modelling of the Impact Crater Depth–Diameter Dependence in an Acoustically Fluidized Target. *Planetary and Space Science* 51: 831–845.

SUPPORTING INFORMATION

Additional supporting information may be found in the online version of this article.

Data S1. iSALE-2D modeling results

Table S1. ANIE data analysis.

Table S2. Statistical analysis of unindexed PDF sets per sample.